Thin–Walled Structures 219 (2026) 114297

Contents lists available at ScienceDirect

Thin-Walled Structures

journal homepage: www.elsevier.com/locate/tws

Full length article

Buckling behaviour and design of DED-Arc high strength steel circular hollow sections

Wenxuan Hong [a], Ruizhi Zhang [a,*], Nicolas Hadjipantelis [b], Leroy Gardner [a]

[a] Department of Civil and Environmental Engineering, Imperial College London, London, SW7 2AZ, United Kingdom
[b] Department of Civil and Environmental Engineering, University of Cyprus, Nicosia, 2109 Aglantzia, Cyprus

ARTICLE INFO

Keywords:
Circular hollow sections
Compression tests
Design recommendations
High strength steel
Metal 3D printing
Shell buckling
Wire arc additive manufacturing
Wire-arc directed energy deposition

ABSTRACT

Wire-Arc Directed Energy Deposition (DED-Arc) or Wire Arc Additive Manufacturing (WAAM) is a metal 3D printing method offering the ability to produce large-scale structural components with complex geometries in an efficient and cost-effective manner. To date, only a limited number of experimental studies on the structural behaviour of slender DED-Arc hollow sections have been conducted. To fill this gap, new experimental evidence on the behaviour of DED-Arc shell structures is thus reported. A comprehensive experimental programme investigating the local buckling response of DED-Arc high strength steel circular hollow sections (CHS) over a wide range of cross-sectional slendernesses has been conducted. In total, twelve DED-Arc CHS stub columns with a series of diameter-to-thickness ratios were produced using ER120S-G wire. The undulating as-built geometry and the initial geometric imperfections of the stub columns were captured using 3D laser scanning. During the stub column tests, the deformation fields were captured by means of digital image correlation. In the present paper, following the description of the specimen production, the experimental programme is described, the test results are analysed and the applicability of the current Eurocode 3 rules to the design of DED-Arc CHS is assessed by comparing the test results with the EN 1993-1-1 and EN 1993-1-6 design provisions. The test results show that the structural behaviour of DED-Arc CHS is similar to that of conventionally-produced (i.e. cold-formed and hot-rolled) steel CHS. Both EN 1993-1-1 and EN 1993-1-6 yield safe-sided resistance predictions, with the latter being more accurate since it incorporates the influences of both the fabrication quality and of the initial geometric imperfections.

1. Introduction

Wire-Arc Directed Energy Deposition (DED-Arc) [1] is a metal 3D printing method that utilises an electric arc in conjunction with robotic equipment to build metal components in a layer-upon-layer manner. DED-Arc offers a high degree of manufacturing freedom in producing intricate and highly customised geometries, thus opening up new opportunities for reduced material consumption and enhanced structural and environmental performance [2–5]. Owing to the high deposition rates (reportedly up to 9.5 kg/h [6]) it offers relative to other metal 3D printing methods, DED-Arc is highly efficient and cost-effective for producing large-scale structural components, making it well-suited for applications in aerospace and structural engineering [7]. DED-Arc has been successfully deployed in many pioneering projects in the aerospace industry, including in the manufacture of fuselage panels and wing spars for aircraft [8,9], supporting structures for satellites [10] and structural components and engine parts for space rockets [11,12], owing primarily to the capability it offers to produce customised components in a monolithic manner without costly moulds, thereby enhancing manufacturing speed and flexibility [13]. Recent applications of DED-Arc have extended into structural engineering, capitalising on the capabilities it offers for manufacturing optimised elements and structures [14–16] and for the ability to repair or strengthen existing structures [15,17–21]. Furthermore, recent studies have explored the concept of exploiting the undulating surface geometry that results from the DED-Arc process to enhance the structural performance of steel–concrete composite circular sections [22–24].

A growing number of studies have investigated the structural behaviour of DED-Arc cross-sections (e.g. angles [25,26], C-sections [27], I-sections [28] and square hollow sections [29–31]). The local buckling modes observed in DED-Arc plated structures have generally been found to resemble the classic local buckling modes of thin-walled cross-sections [26–28,30], but with some interference from the initial geometric imperfections and the surface undulations inherent to the DED-Arc process [25,29,32]. Furthermore, the load-carrying capacities

* Corresponding author.
E-mail address: ruizhi.zhang@imperial.ac.uk (R. Zhang).

https://doi.org/10.1016/j.tws.2025.114297
Received 3 September 2025; Received in revised form 9 November 2025; Accepted 22 November 2025
Available online 24 November 2025
0263-8231/© 2025 The Authors. Published by Elsevier Ltd. This is an open access article under the CC BY license (http://creativecommons.org/licenses/by/4.0/).

of the majority of the tested DED-Arc specimens reported in the literature followed the trend of the test data on conventionally-produced cross-sections [28–30], though some specimens with pronounced local imperfections exhibited inferior structural performance [25,30].

While exploitation of the geometric flexibility of DED-Arc to manufacture structurally-optimised elements is key to its viability in practice, it is also important to understand and benchmark the performance of regular cross-sections, which themselves may form part of optimised structures. Tubular elements are a mainstay of structural engineering, with cross-sections typically having square, rectangular, circular, elliptical or some other novel profiles [33–38]. In the case of circular hollow sections (CHS), particularly those of slender proportions, the local buckling behaviour is sensitive to initial geometric imperfections [39,40]. To date, limited attention has been given to exploring the structural behaviour of DED-Arc CHS (e.g. [41,42]), especially slender profiles, despite a wide range of potential applications, such as space rockets, aircraft and structural elements. Consequently, there is a dearth of relevant experimental data. Thus, in the present study, benchmark testing on DED-Arc CHS is conducted to assess both their buckling response and the associated design resistance predictions, relative to conventionally-produced CHS. The experimental programme comprised characterisation of the material microstructure, tensile coupon tests for the determination of the mechanical properties, initial geometric imperfection measurements using 3D laser scanning and stub column tests to examine the local buckling behaviour and compressive resistance of DED-Arc high strength steel CHS covering a wide range of diameter-to-thickness ratios. Digital image correlation (DIC) was used during testing to monitor the surface deformations of the coupons and stub column specimens. The test results were analysed and were compared (alongside existing test data) with the design resistance predictions obtained using EN 1993-1-1 [43] and EN 1993-1-6 [44].

2. Specimen production and preparation

Twelve CHS and two flat-sided ovals were manufactured at the DED-Arc facility of the Steel Structures Laboratory of the University of Cyprus, using an ABB 6-axis robotic arm in conjunction with an Oerlikon Citowave II 520 welding power source, shown in Fig. 1. The manufacturing process and the calibration of the process parameters followed the guidelines by Hadjipantelis [45]. Grade ER120S-G high strength welding wire with a 0.8 mm diameter was adopted as the feedstock material; its chemical composition and nominal mechanical properties are listed in Tables 1 and 2, respectively. The CHS specimens and flat-sided ovals were produced with a nominal thickness of 2.2 mm using the process parameters listed in Table 3. All the specimens were printed using a single pass deposition strategy, with randomised start points and alternating deposition directions between layers. The CHS specimens were printed in three batches, with the total deposition length per layer in each batch designed to be similar to that of the two flat-sided ovals, ensuring comparable cooling times across all specimens. During printing, the welding current and voltage at each coordinate of the geometry were logged at a 5 kHz frequency using a smart sensor network. The logged values were used to calculate the actual heat input of the printing process [45]; this was performed by determining the average instantaneous power [46–48] based on the entire dataset, multiplying it by the thermal efficiency factor (taken as 0.8 herein [49]) and dividing it by the travel speed. As shown in Fig. 2, where the variation of the average actual heat input across each printed layer of a typical specimen is presented, the heat input was fairly consistent along the entire height of the specimens, thus indicating a consistent printing process [45].

The DED-Arc CHS specimens were labelled starting with the cross-section shape ('C' for CHS), followed by the test type ('S' for stub column test) and the nominal outer diameter (in mm). For instance, 'CS400' represents the CHS stub column with a nominal outer diameter of 400 mm. The specimen IDs of the examined CHS stub column specimens are CS20, CS30, CS40, CS55, CS80, CS110, CS150, CS200, CS250, CS300, CS350 and CS400. The DED-Arc process was programmed, controlled and monitored using the DED-Arc-dedicated software MetalXL [50]. Four flat plates were extracted from the flat-sided ovals using a bandsaw. Twenty-six tensile coupon specimens were then machined from the flat plates using water jet cutting, with three different coupon orientations, namely θ = 0°, 45° and 90°, as shown in Fig. 3. The different coupon orientations enabled possible anisotropy within the DED-Arc material to be assessed; the nominal dimensions of the tensile coupons were in accordance with EN ISO 6892-1:2019 [51], as shown in Fig. 3. The coupon specimens were sandblasted with garnet abrasive to clean the surfaces. To evaluate the influence of the geometric undulations of the as-built geometry on the mechanical properties, ten coupon specimens were machined to a uniform thickness, as demonstrated in Fig. 4(a); a typical as-built surface finish of the DED-Arc CHS stub column specimens is shown in Fig. 4(b).

Table 1
Chemical composition (in % by weight) of the ER120S-G wire, as reported in the wire certificate.

C	Si	Mn	P	S	Cr	Ni	Mo	Nb	Cu	V
0.01	0.11	0.84	1.79	0.005	0.012	0.36	2.24	0.57	< 0.01	0.01
Ti	Al	B	Co	As	Sn	Sb	Pb	Zr	Fe	
0.091	0.005	0.001	0.001	0.002	0.005	< 0.001	0.002	0.002	Balance	

The steps followed for the preparation of the DED-Arc CHS stub columns are shown in Fig. 5. The CHS specimens were first cut to length using a bandsaw, then faced on a lathe to achieve flat and square ends, and finally sandblasted with 0.3 mm garnet abrasive to remove rust and welding soot from the manufacturing. The stub column lengths L were determined as a multiple k of the half-wavelength of the axisymmetric elastic buckling mode λ_{axi} of a thin cylindrical shell under axial compression [39], as given by Eq. (1):

$$L = k\lambda_{axi} = \frac{k\pi\sqrt{rt}}{\left[12\left(1-\nu^2\right)\right]^{1/4}}, \tag{1}$$

where r is the radius of the middle surface of the cylindrical shells, t is the shell thickness, and ν is the Poisson's ratio. A sensitivity study on specimen lengths was carried out using finite element analysis, adopting the same approach as employed by Zhang et al. [52]. Following the geometrically and materially nonlinear analysis with imperfections (GMNIA) conducted on all the cross-section profiles, specimen lengths equal to eight half-wavelengths (i.e. k = 8) were deemed suitable, at which lengths the ultimate capacities obtained from GMNIA converged. The specimen lengths were thus sufficiently long to avoid restraining effects from the fixed boundary conditions and to preserve typical local geometric imperfections (see Section 3.4), while remaining short enough to prevent global buckling. It should be noted that the value of k can vary for different cross-sectional profiles and materials; thus, the aforementioned procedure would need to be repeated in other cases to determine the suitable column length. The prepared DED-Arc CHS specimens are shown in Fig. 6 with increasing cross-sectional slenderness from left to right and front to back.

3. Geometric analysis

As described in the present section, 3D laser scanning was employed to capture the geometries of both the tensile coupons and the CHS specimens. Geometric analysis was then performed to determine their geometric properties and characterise the surface undulations of the DED-Arc surfaces. Archimedes' principle was employed to determine the density of the examined DED-Arc material and to verify the accuracy of the scan data. The geometric properties of the machined tensile coupons (i.e. the width and thickness within the parallel length) were measured using a digital calliper.

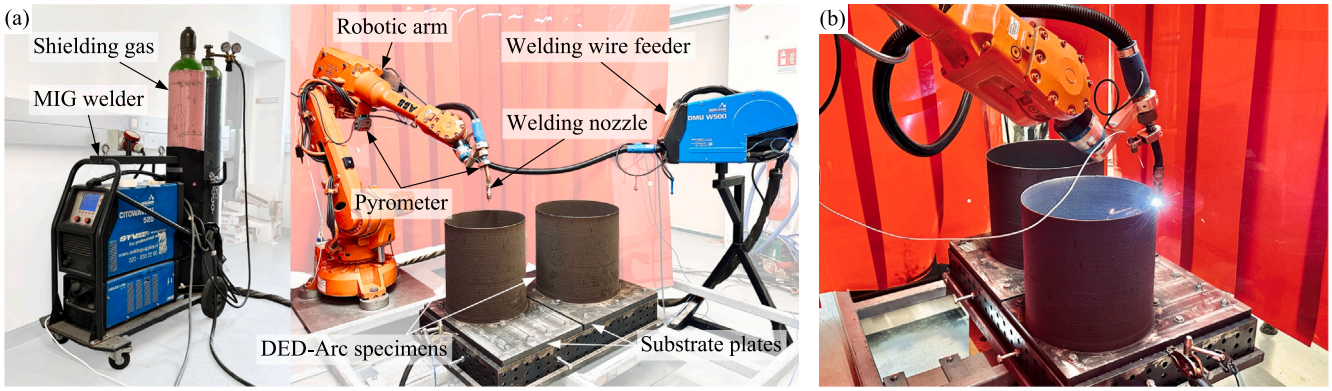


Fig. 1. (a) DED-Arc setup used for specimen production; (b) printing of the DED-Arc CHS specimens.

Table 2
Nominal mechanical properties (all weld metal) of the ER120S-G wire, as reported in the wire certificate.

Condition	0.2% proof strength (MPa)	Ultimate strength (MPa)	Fracture strain (%)	Impact energy (–)
As-welded	890	950	15	70 J at −40 °C; 50 J at −60 °C

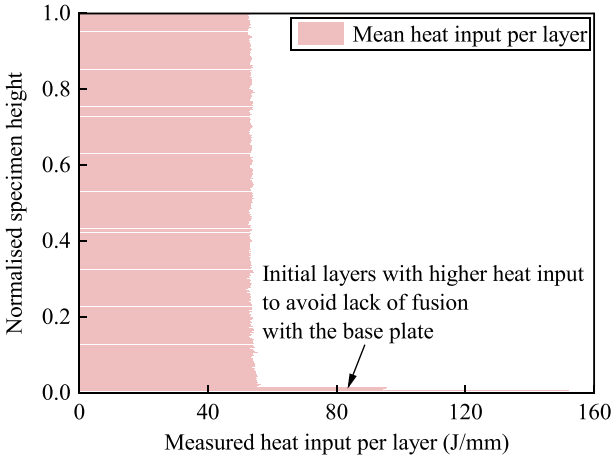


Fig. 2. Measured heat input at each layer along the specimen height of a typical DED-Arc CHS stub column specimen.

Table 3
Process parameters adopted for manufacturing of the oval and CHS specimens.

Process parameter	Details
Feedstock wire	ER120S-G
Wire diameter (mm)	0.8
Wire feed speed (m/min)	2.0
Travel speed (mm/s)	7.5
Nominal deposition rate (kg/h)	0.47
Contact tip-to-work distance (mm)	11.0
Nominal current (A)	35.0
Nominal voltage (V)	14.0
Nominal heat input[a] (J/mm)	52.3
Actual heat input (J/mm)	53.4
Maximum interpass temperature (°C)	250
Shielding gas composition	82%Ar–18%CO_2
Gas flow rate (L/min)	16
Welding mode	Short circuiting transfer
Cooling method	Passive cooling
Nominal thickness (mm)	2.2
Average thickness (mm)	2.13
Average layer height (mm)	1.024

[a] Assumes thermal efficiency factor of 0.8 for Metal Inert Gas welding [49].

3.1. Density measurements

Samples for density measurements were cut from different locations on the plates. By employing Archimedes' principle, the measurements were carried out with the setup and procedure shown in Fig. 7. First, the mass of the density sample was measured using a digital scale. Then, hung by a string, the density sample was placed in a measuring cylinder filled with water and placed on the scale. The change in the scale reading after the sample was submerged in the water Δm was considered to be the mass corresponding to the buoyancy force (which is equal to the weight of the water of the same volume as the submerged object) exerted on the sample. The volume of the submerged sample $V_{specimen}$ was thus obtained by dividing the mass change Δm by the water density ρ_{water}. The average density of the examined DED-Arc material was 7.822 g/cm^3, which is similar to the DED-Arc high strength steel densities reported by Huang et al. [53] and Weber et al. [54], and is marginally lower than the standard value of 7.85 g/cm^3 for carbon steels [55].

3.2. 3D laser scanning

A FARO ScanArm integrated with a line laser probe capable of scanning with an accuracy of 0.1 mm at a point acquisition rate of 500,000 points per second [56] was used for the 3D laser scanning procedure, with the setup shown in Fig. 8. A magnetic base was used to fix the DED-Arc specimens in position to prevent movement during scanning. The obtained point clouds were gridded with a spacing of 0.1 mm leading to at least 10 points across each printed layer and thus an accurate representation of the surface undulations. The volumes measured from the scanned data were compared to the volumes calculated by dividing the mass of the specimens by the measured density $\rho_{specimen}$, as detailed in Section 3.1. The resulting discrepancies were found to be less than 1%, indicating high accuracy in the laser scan data. The point clouds were initially processed in the software Geomagic Wrap [57], then exported as polygon meshes in a .STL file format, and imported into the software Rhino [58] and MATLAB [59] for geometric analysis.

3.3. DED-Arc as-built coupons

The full geometries of the as-built tensile coupons were analysed as shown in Fig. 9. To position the coupon centroid at the origin of

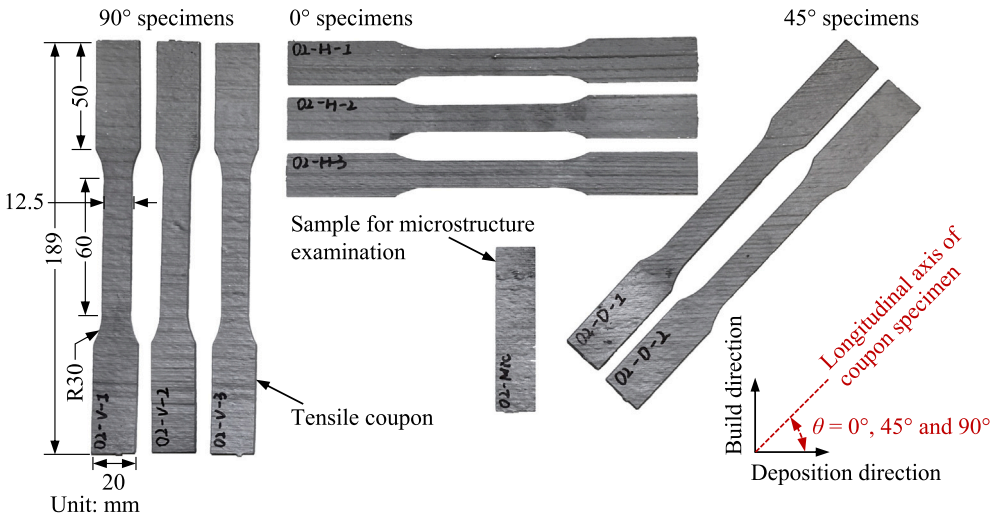


Fig. 3. Orientation of the tensile coupon specimens relative to the deposition direction.

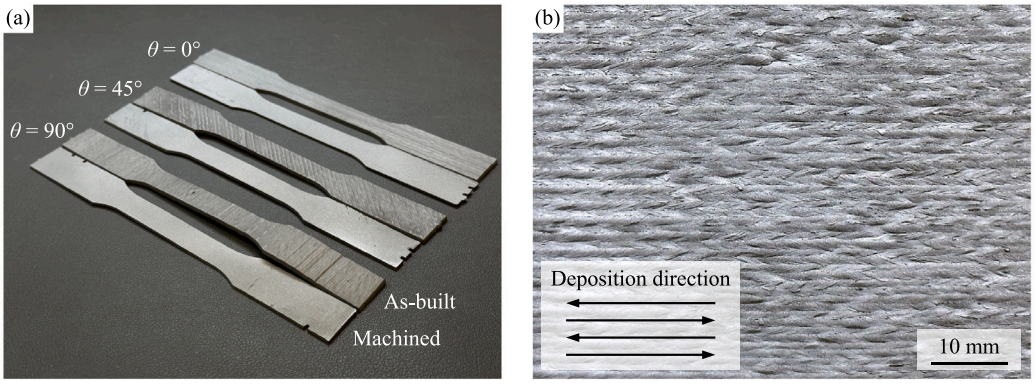


Fig. 4. (a) Typical as-built and machined tensile coupons; (b) typical surface finish of the DED-Arc CHS stub columns.

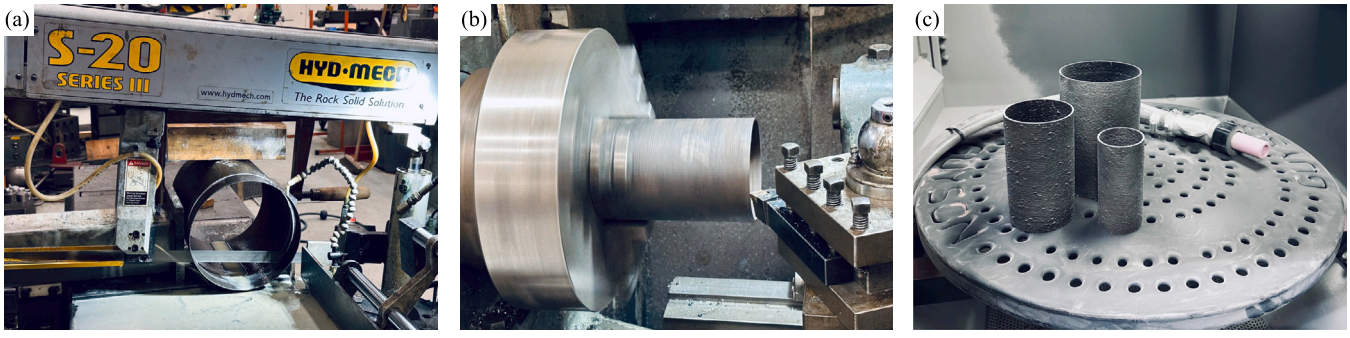


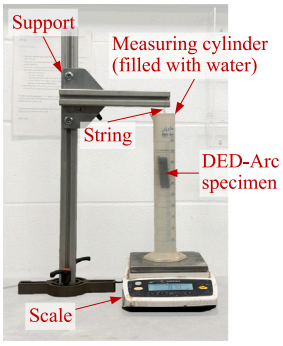
Fig. 5. Preparation of DED-Arc CHS stub column test specimens: (a) bandsaw cutting; (b) end flattening using a lathe; (c) sandblasting with garnet abrasive.

the global coordinate system and to align the longitudinal axis of the parallel length of the coupon with the global x axis, the scan data were orientated in Rhino [58] using principal component analysis [60]. A series of contours were created along the parallel length of the coupons with a spacing dx, based on which the cross-sectional area A_i and the eccentricities of the cross-sectional centroid relative to the overall coupon centroid along the global y and z axes ($|e_{y,i}|$ and $|e_{z,i}|$, respectively) were obtained. Subsequently, contours were created across the coupon width with a spacing dy to obtain the grid points from which the local thickness t_{ij} was measured, as illustrated in Fig. 9.

A sensitivity study was conducted for six as-built coupons with three different coupon orientations to determine the values of dx and dy that would capture the features of the as-built surfaces at a reasonable computational cost. For simplicity, the same contour spacing s was applied along both the x and y axes (i.e. s = dx = dy); the spacing values of 0.05 mm, 0.1 mm, 0.5 mm, 1.0 mm and 2.0 mm were investigated. The results of the sensitivity study are summarised in Fig. 10, showing the average and minimum cross-sectional area (denoted by A and A_{min}, respectively), average and minimum thickness (denoted by t and t_{min}, respectively), and average and maximum eccentricity (denoted by $|e_z|$ and $|e_z|_{max}$, respectively), normalised by their corresponding values when s = 0.05 mm. All geometric measurements had essentially converged at s = 0.1 mm; this spacing was therefore selected for the geometric analysis of all specimens.



Fig. 6. DED-Arc CHS specimens for stub column testing.



Procedure:

1. Mass of specimen: $m_{specimen}$
2. Increase in scale reading, when specimen is submerged: Δm
3. Volume of specimen: $V_{specimen} = \Delta m / \rho_{water}$
4. Density of specimen: $\rho_{specimen} = m_{specimen} / V_{specimen}$

Fig. 7. Setup and procedure for density measurements based on Archimedes' principle.

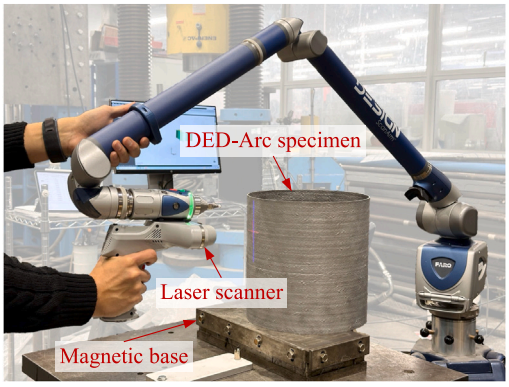


Fig. 8. 3D laser scanning of typical DED-Arc CHS stub column.

The geometric properties of the as-built coupons, including the standard deviation of the cross-sectional area A_{sd}, the standard deviation of the thickness t_{sd} and the standard deviation of the eccentricity along the z axis $|e_z|_{sd}$ are reported in Table 4. Histograms of the measured local thicknesses t_{ij} and cross-sectional areas A_i (normalised by t and A, respectively) of three typical as-built coupons of different orientations, are shown in Fig. 11. Fig. 11(a) shows consistent thickness distribution patterns across coupons with varying orientations. The variation of the cross-sectional area was found to increase with the coupon orientation angle, as indicated by the higher A_{sd} values and the spread of A_i, as shown in Fig. 11(b). This is because the higher the angle θ, the greater the number of contours that were made across crest and trough regions, thus leading to higher cross-sectional area variation. Owing to the surface undulations along the build direction, $|e_z|$ was found to be greater than $|e_y|$ for coupons with $\theta = 45°$ and $\theta = 90°$, while for coupons with $\theta = 0°$, $|e_z|$ and $|e_y|$ were similar. Similar findings have been reported by Weber et al. [54] and Chen et al. [61].

Table 4
Geometric properties of the as-built coupons.

Coupon ID	A (mm^2)	$\frac{A_{min}}{A}$	$\frac{A_{sd}}{A}$	t (mm)	$\frac{t_{sd}}{t}$	$\frac{\lvert e_y\rvert}{t}$	$\frac{\lvert e_z\rvert}{t}$	$\frac{\lvert e_z\rvert_{max}}{t}$	$\frac{\lvert e_z\rvert_{sd}}{t}$
AB-0-1	26.8	0.98	0.010	2.12	0.038	0.119	0.008	0.030	0.008
AB-0-2	26.3	0.96	0.018	2.14	0.051	0.067	0.072	0.083	0.005
AB-0-3	25.9	0.97	0.013	2.11	0.046	0.023	0.006	0.015	0.003
AB-0-4	26.7	0.97	0.013	2.15	0.050	0.057	0.038	0.059	0.009
AB-0-5	26.2	0.97	0.012	2.13	0.032	0.047	0.027	0.046	0.007
AB-0-6	25.7	0.97	0.011	2.09	0.036	0.036	0.005	0.013	0.003
AB-45-1	26.7	0.95	0.021	2.16	0.044	0.029	0.191	0.374	0.122
AB-45-2	25.9	0.96	0.020	2.12	0.038	0.039	0.337	0.471	0.123
AB-45-3	26.8	0.97	0.017	2.16	0.038	0.019	0.139	0.244	0.068
AB-45-4	26.0	0.97	0.012	2.13	0.035	0.020	0.225	0.398	0.128
AB-90-1	27.1	0.92	0.025	2.15	0.038	0.064	0.308	0.523	0.159
AB-90-2	27.6	0.94	0.028	2.14	0.049	0.041	0.277	0.617	0.184
AB-90-3	26.8	0.94	0.021	2.15	0.033	0.093	0.646	0.841	0.113
AB-90-4	27.8	0.93	0.028	2.13	0.045	0.028	0.067	0.124	0.028
AB-90-5	26.2	0.91	0.030	2.11	0.059	0.034	0.479	0.824	0.221
AB-90-6	26.4	0.93	0.030	2.11	0.048	0.038	0.326	0.576	0.131

3.4. DED-Arc CHS stub columns

For the DED-Arc CHS column specimens with an outer diameter larger than 55 mm (i.e. CS80–CS400), both the outer and the inner surfaces were fully captured by the 3D laser scanner. For specimens CS20–CS55, while the outer surfaces were fully captured, the inner surfaces could only be captured near the specimen ends. A similar contouring approach to that followed for the as-built coupons was also used for the CHS stub columns, as outlined in Fig. 12. A linear reference line was established by connecting the centroids of the two outer contours at the ends of the specimen; the perpendicular distance of the centroids of other outer contours to this reference line was defined as the eccentricity e_i, as shown in Fig. 12(a). Furthermore, a centreline was created based on each pair of outer and inner contours along the specimen. Subsequently, the outer contours, inner contours and centrelines were gridded radially at 1° intervals around the circumference to obtain grid points for the determination of the local outer diameter D_{ij} and local wall thickness t_{ij}, as illustrated in Fig. 12(a). The initial geometric imperfections were determined with the method illustrated in Fig. 12(b); a straight line was fitted through each set of the

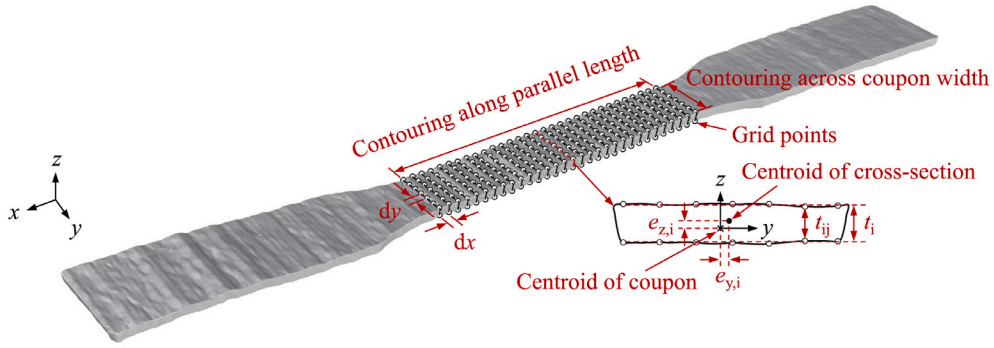


Fig. 9. Geometric analysis of typical tensile coupon in Rhino [58].

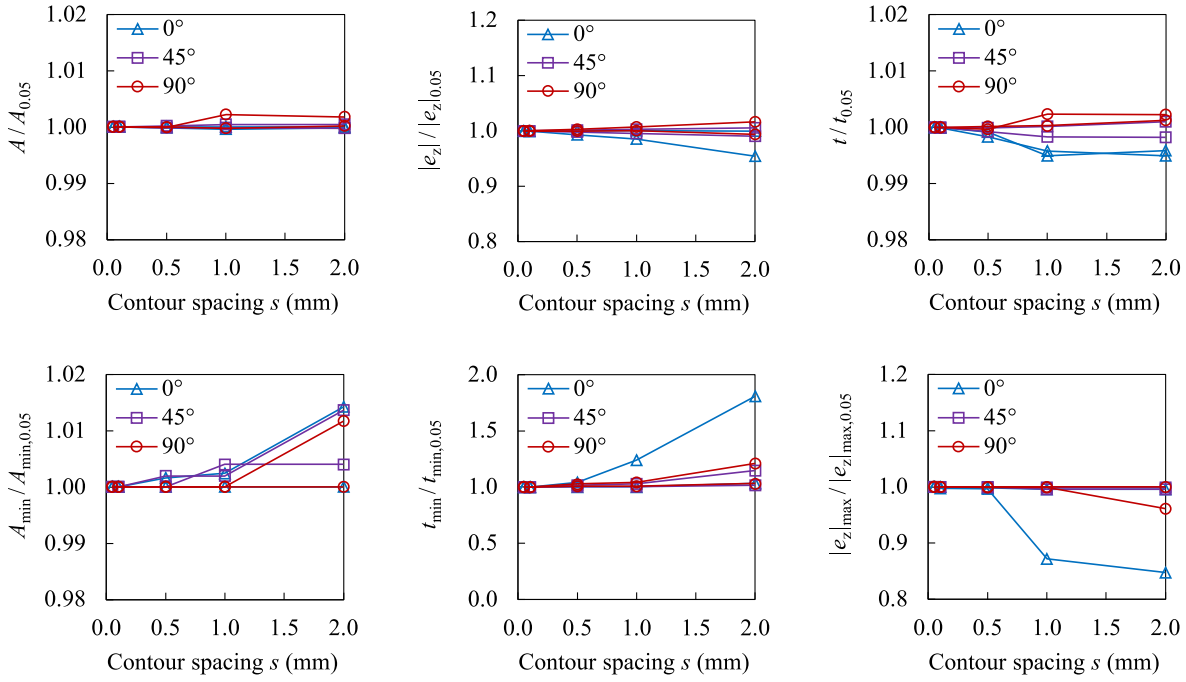


Fig. 10. Results of sensitivity study on contour spacing.

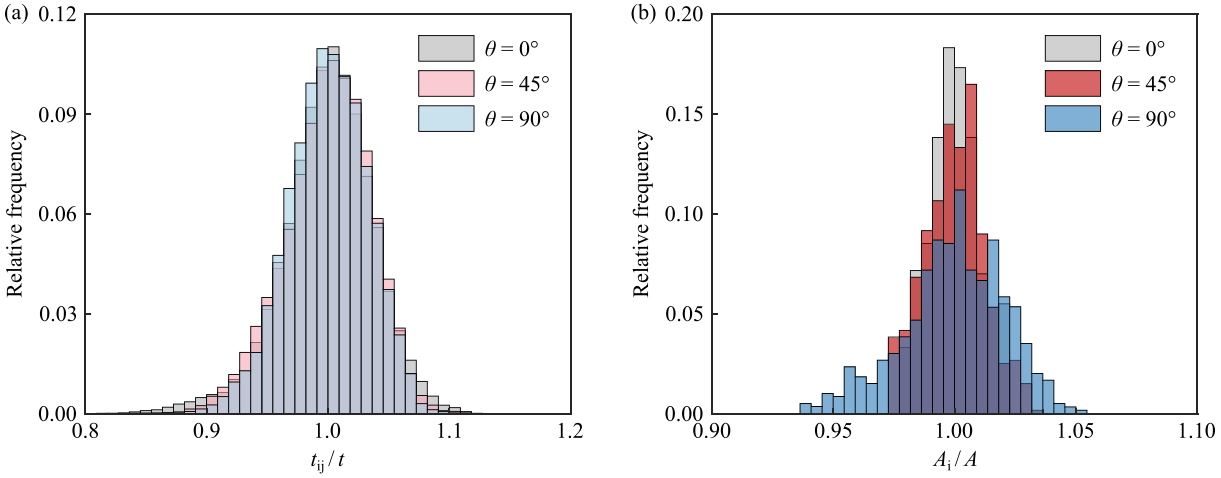


Fig. 11. Histograms of normalised key geometric parameters for typical as-built coupons (i.e. AB-0-1, AB-45-1 and AB-90-1): (a) normalised thickness and (b) normalised cross-sectional area.

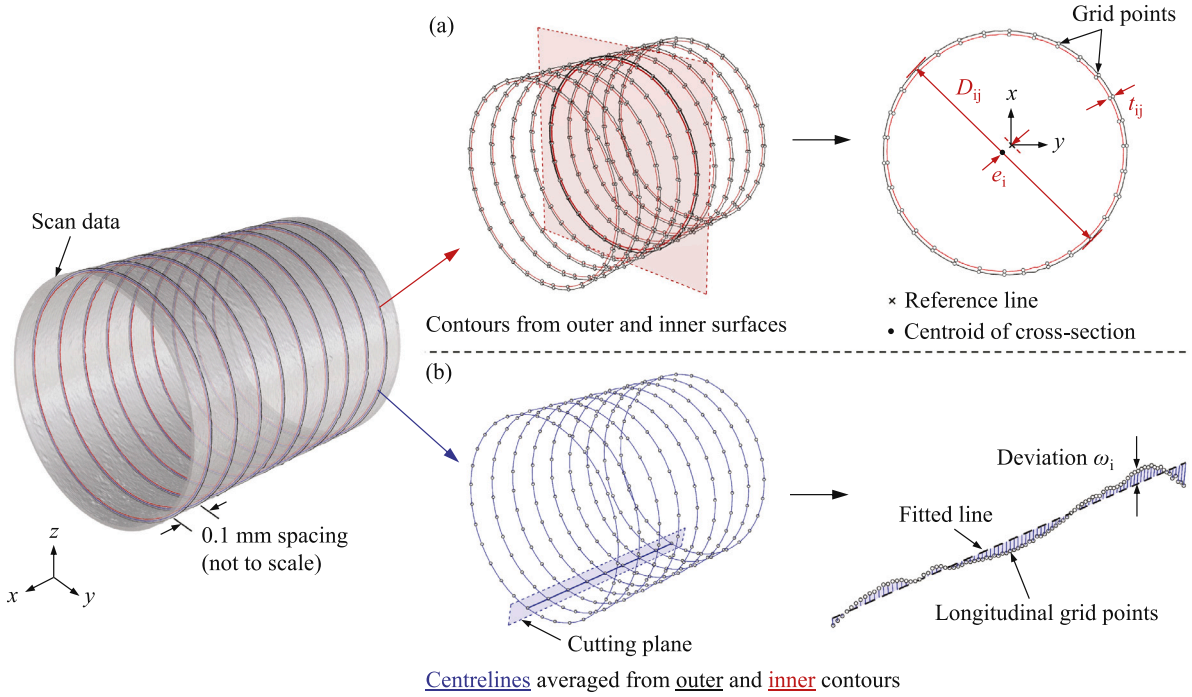


Fig. 12. Geometric analysis of typical DED-Arc CHS stub column: (a) geometric measurements; (b) determination of longitudinal imperfection amplitude.

longitudinal grid points made on the centrelines, and the perpendicular distance of the grid points relative to the fitted line was determined and taken as the longitudinal imperfections ω_i. Note that for specimens CS20–CS55, A_i and t_{ij} were determined only in the regions where the inner scans were available, while their longitudinal imperfections were determined only based on the outer surfaces with the undulations having been smoothed using the same method as employed in [30]. Having conducted a sensitivity study, the size of the smoothening window was determined to be 8 × 8 mm (i.e. approximately equal to the height of eight layers) for specimens CS20–CS55. The CHS specimen length L was obtained by averaging the measurements taken at 30° increments radially around the perimeter of the specimens using a digital height gauge. The average cross-sectional areas $A_{density}$ were also derived using the mass of the specimen M measured with a digital scale, the average density of the examined DED-Arc material $\rho_{specimen}$ and the specimen length L, as given by Eq. (2):

$$A_{density} = \frac{M}{\rho_{specimen} L}. \tag{2}$$

The key geometric properties of the CHS specimens, including the average outer diameter D, the maximum and minimum outer diameters (denoted by D_{max} and D_{min}), the average thickness t, the average and maximum eccentricities from the reference line (denoted by e and e_{max}) and the average cross-sectional areas derived from the scan data A, are reported in Table 5. The differences between the cross-sectional areas derived from the scan data A and the density $A_{density}$ of the specimens with the complete inner scans were on average less than 1%; therefore, $A_{density}$ was adopted herein. For three typical CHS specimens, the normalised deviations between the diameter and area measurements at each contour (i.e. D_i and A_i) and the average values (i.e. D and A), defined as $\Delta D_i/D$ and $\Delta A_i/A$, respectively, are plotted against the normalised position along the columns in Fig. 13. End flaring can be observed from the results shown in Fig. 13(a), which is attributed to the release of bending residual stresses, as similarly observed in additively manufactured and conventional cold-formed circular hollow sections [62,63]. The histograms of the diameter, thickness and area measurements in Fig. 14 reveal that the geometric properties of the DED-Arc CHS specimens generally follow a normal distribution.

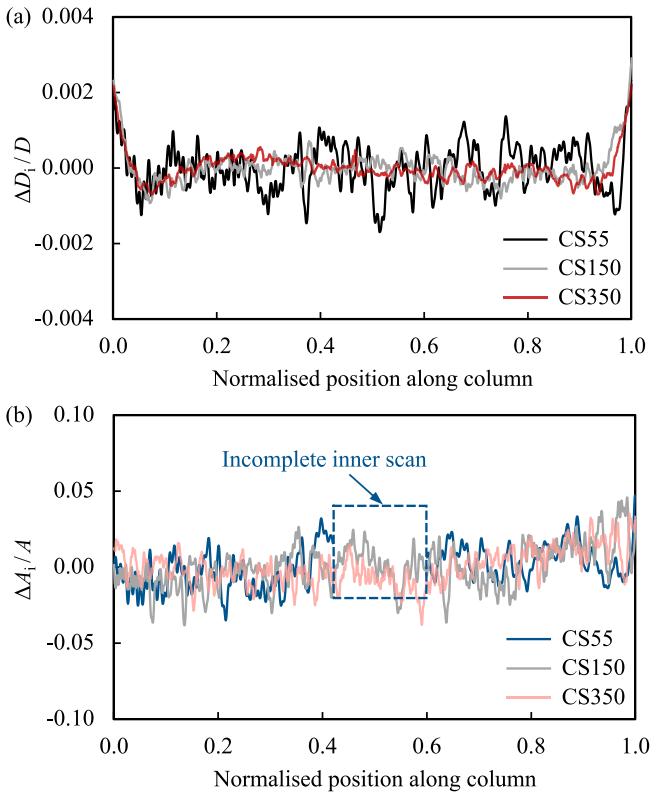


Fig. 13. Distributions of (a) normalised deviation of diameter $\Delta D_i/D$ and (b) normalised deviation of cross-sectional area $\Delta A_i/A$ along typical stub column specimens.

The measured initial geometric imperfections include longitudinal imperfections and out-of-roundness, in line with EN 1993-1-6 [44]. The method utilised for analysing the longitudinal imperfections has

Table 5
Geometric properties of the CHS stub column specimens.

Specimen ID	D (mm)	D_{max} (mm)	D_{min} (mm)	t (mm)	e (mm)	e_{max} (mm)	L (mm)	A (mm^2)	$A_{density}$ (mm^2)	$\frac{A}{A_{density}}$
CS20	19.16	20.89	18.52	2.17	0.09	0.20	64.93	115.0	118.2	0.973
CS30	29.23	30.09	28.66	2.19	0.07	0.15	81.31	185.4	185.1	1.001
CS40	39.20	39.95	38.67	2.21	0.05	0.11	94.77	256.0	251.6	1.017
CS55	54.14	55.16	53.51	2.15	0.05	0.11	112.17	351.2	349.6	1.005
CS80	79.04	79.88	78.37	2.15	0.09	0.16	137.02	518.8	515.5	1.006
CS110	108.86	110.19	108.11	2.12	0.08	0.17	160.20	710.1	713.6	0.995
CS150	148.51	149.74	147.64	2.12	0.05	0.10	187.88	972.9	978.1	0.995
CS200	198.24	199.81	197.53	2.12	0.11	0.34	201.54	1303.7	1299.7	1.003
CS250	247.95	250.43	247.26	2.09	0.14	0.32	250.38	1615.1	1630.3	0.991
CS300	297.44	299.58	296.67	2.09	0.16	0.38	275.67	1942.6	1961.3	0.990
CS350	347.32	349.94	346.48	2.12	0.17	0.40	291.17	2300.8	2301.8	1.000
CS400	396.79	399.22	395.48	2.13	0.12	0.46	313.11	2635.0	2641.7	0.997

been described above. Fig. 15 shows the distribution of the longitudinal imperfections in specimen CS300, where the outward and inward deviations are assigned positive and negative values, respectively. The longitudinal imperfection amplitudes measured over the full length of the specimens and the length between the ring stiffeners (see Section 5) are denoted by $\omega_{l,full}$ and ω_l, respectively. A histogram of the maximum local imperfection amplitude (between the ring stiffeners) around the circumference of a typical column specimen (CS400) is plotted in Fig. 16 alongside the corresponding empirical cumulative distribution function (CDF) curve. For each column specimen, appropriate percentile imperfection amplitudes were taken as $\omega_{l,full}$ and ω_l (rather than adopting the maximum amplitudes), to eliminate the influence of significant weld beads and data noise, which are interpreted as statistical outliers relative to the main distribution, as shown in Fig. 16. The values of ω_l and $\omega_{l,full}$ of all specimens are shown in Table 6; the ω_l values were deemed to be more appropriate to represent the local imperfection amplitudes since they exclude the influence of the flared ends that are restrained by the ring stiffeners. Typically, the local geometric imperfection patterns observed in the DED-Arc CHS specimens can be characterised by a series of short waves along the build direction, with a few distinct waves (shifted layers or higher amplitudes) resulting from technical inconsistency during the printing process. These patterns are different from the sinusoidal local imperfection patterns with somewhat longer wavelengths that are commonly seen in conventionally-produced (i.e. cold-formed [62,64] and hot-rolled [64]) steel CHS.

The out-of-roundness at each contour of the outer surface, denoted as O_i, was calculated using Eq. (3):

$$O_i = \frac{D_{i,max} - D_{i,min}}{D_i}, \tag{3}$$

where $D_{i,max}$, $D_{i,min}$ and D_i are the maximum, minimum and average diameters of the contours, respectively. The maximum measured out-of-roundness values O_{max} of all specimens are listed in Table 6. The fabrication quality of the specimens was evaluated in accordance with EN 1993-1-6 by categorising the local imperfection amplitude ω_l and the maximum out-of-roundness O_{max} in Classes A–D. To determine the boundary values of the imperfections between the fabrication classes [44], the shell local imperfection amplitude δ_0 was determined using Eq. (4):

$$\delta_0 = \frac{1}{Q_\omega}\sqrt{rt}, \tag{4}$$

where Q_ω represents the fabrication quality parameter, i.e. 40, 25 and 16 for Classes A, B and C, respectively [44]. For circular shells with an outer diameter of 0.5 m or less, the recommended tolerances of out-of-roundness O are 0.014, 0.020 and 0.030 for fabrication Classes A, B and C, respectively [44]. Those specimens whose local imperfection amplitude or out-of-roundness exceed the Class C tolerances are deemed to be Class D. The fabrication qualities derived from the local imperfection amplitude and the maximum out-of-roundness (denoted by Q_{ω_l} and $Q_{O_{max}}$, respectively) for each test specimen are listed in Table 6. Overall, the specimens with larger cross-sections exhibited a higher fabrication quality regarding the degree of out-of-roundness but lower fabrication quality regarding the local imperfection amplitude. This is because slender specimens are more susceptible to thermally-induced deformations during cooling owing to their lower stiffness; thus, the residual stresses lead to larger layer misalignment and, consequently, larger local imperfection amplitudes.

Table 6
Measured geometric imperfection amplitudes, out-of-roundness and fabrication quality classes of DED-Arc CHS test specimens.

Specimen ID	ω_l (mm)	$\omega_{l,full}$ (mm)	O_{max} (–)	Q_{ω_l} (–)	$Q_{O_{max}}$ (–)
CS20	0.202	0.202	0.100	C	D
CS30	0.135	0.135	0.041	A	D
CS40	0.142	0.142	0.028	A	C
CS55	0.145	0.145	0.023	A	C
CS80	0.293	0.345	0.015	B	B
CS110	0.297	0.351	0.016	B	B
CS150	0.300	0.374	0.010	A	A
CS200	0.377	0.506	0.010	B	A
CS250	0.432	0.543	0.011	B	A
CS300	0.444	0.560	0.009	B	A
CS350	0.581	0.667	0.009	B	A
CS400	0.469	0.772	0.007	A	A

4. Material tests

Microstructural and tensile coupon tests were performed to investigate the material behaviour of the DED-Arc high strength steel. The microstructural characterisation was conducted using a scanning electron microscope (SEM) and electron backscatter diffraction (EBSD) in the Centre for Infrastructure Materials, while the tensile coupon tests were conducted in the Structures Laboratory, both in the Department of Civil and Environmental Engineering at Imperial College London.

4.1. Microstructural characterisation

Three small metallographic samples for microstructural examination were extracted from the central region of the DED-Arc plates and were prepared in accordance with ASTM E3-11 [65]. The SD and TD axes of the metallographic samples were aligned in parallel and transversely to the print layers, respectively, while the BD axis was aligned with the build direction, as shown in Fig. 17. The samples were mounted in Bakelite with the front, side and cross-section faces (i.e. the SD-BD, TD-BD and SD-TD planes) exposed, before being ground using silicon carbide abrasive papers ranging from 500, 800, 1200 to 2000 grit, followed by a polishing sequence utilising 6, 3 and 1 μm diamond suspensions and finally a mixture of OP-S colloidal silica solution to achieve a mirror finish. The polished surfaces were

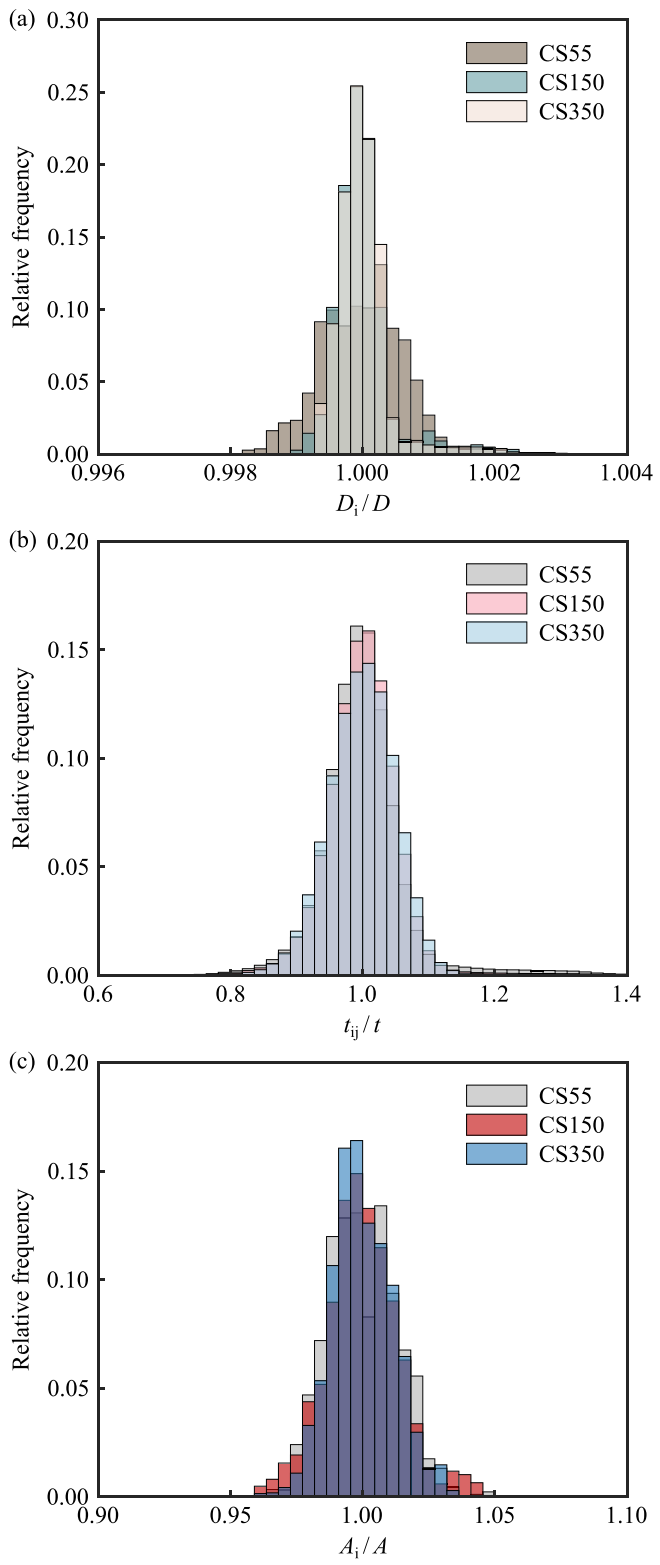


Fig. 14. Histograms of normalised key geometric parameters for typical stub column specimens: (a) normalised diameter D_i/D, (b) normalised thickness t_{ij}/t and (c) normalised cross-sectional area A_i/A.

meticulously cleaned with acetone to remove any contaminants and residual reagents. Subsequently, the prepared samples were inspected under an optical microscope to ensure that no visible contamination or scratches were present prior to the SEM and EBSD examinations.

The EBSD measurements were conducted to reveal the crystallographic texture and the grain morphology of the material using a Zeiss Sigma-500 SEM with an Oxford Instruments Symmetry EBSD detector operating at a 20 kV electron beam acceleration voltage. The samples were pre-tilted at 70° relative to the horizontal and were scanned at a magnification of 1000× over an area of 115 × 87 μm^2 to capture a sufficient number of grains, while preserving the sub-structure details of the examined material. The EBSD patterns were acquired with a minimum 90% indexing using the acquisition software Oxford Instruments AZtec [66] and reconstructed through grain dilation and segmentation using the MATLAB toolbox MTEX 5.6.0 [67].

The scans captured approximately 3000 grains. Typical EBSD results of the front (SD-BD) and cross-section (SD-TD) faces are shown in Fig. 18, including the inverse pole figures (IPFs) of the SD-BD face and the SD-TD face, coloured relative to the build direction and the deposition direction, respectively, and {100}, {110} and {111} pole figures of the SD-BD face. The colour scheme in the IPF map represents the orientation of the grains. In the pole figures, the crystallographic orientations of all the grains in the sample coordinate system are summarised. The results demonstrate that the examined DED-Arc high strength steel exhibited an overall weak texture with no preferred crystallographic orientation, indicating nearly isotropic elastic material behaviour is to be expected.

The distributions of the grain size, defined as the diameter of an equivalent circle with the same area, are shown in Fig. 19(a), where it is observed that a large fraction of grains ranged from 1 to 6 μm, with an average size of 1.64 μm and 1.67 μm in the front and cross-section samples, respectively. The grain aspect ratio, defined as the ratio of the major and minor axis lengths of an equivalent ellipse fitted to each grain [68] was also measured; its distribution is shown in Fig. 19(b). Unlike the equiaxed shape observed in DED-Arc normal strength steels [69,70], the DED-Arc ER120S-G steel exhibited slightly elongated grain shapes with an average grain aspect ratio larger than 2.4. Similar microstructural characteristics to the aforementioned have been reported by Weber et al. [54], Chen et al. [61] and Huang et al. [71].

4.2. Tensile coupon tests

Tensile coupon tests were performed at room temperature in accordance with EN ISO 6892-1:2019 [51]. The test setup is shown in Fig. 20. An Instron 8802 250 kN hydraulic testing machine equipped with hydraulic grips was used. Before testing, a series of overlapping standard gauge lengths equal to 50 mm [51] was marked on the side faces of each coupon using a metal scribe to measure the standard fracture strain. The parallel length of the coupon faces was painted matt black and then spray-painted with a random white speckle pattern. To monitor the displacement fields during testing, a four-camera stereoscopic LaVision digital image correlation (DIC) system [72] was used, featuring two cameras and an integrated LED illumination source on each side.

The tests were conducted under displacement control at a strain rate of 0.007% s^{-1} up to the upper yield strength, and at 0.025% s^{-1} from yielding to failure, with a gradual transition through three intermediate steps [51]. The applied load was measured by a load cell built into the testing machine and transmitted to the DIC system, and recorded synchronously with the DIC images at a frequency of 1 Hz using the software DaVis 10 [73]. After the tests, the DIC images were processed in DaVis 10 [73] to analyse the strain fields along the full parallel length of both faces of the coupons. The stress–strain curves were taken as the average of the two sides of the coupons; the stress was calculated as the applied load divided by the average original cross-sectional area, while the average axial strain was computed over the entire parallel length. A similar test setup and procedure was successfully employed in [74,75].

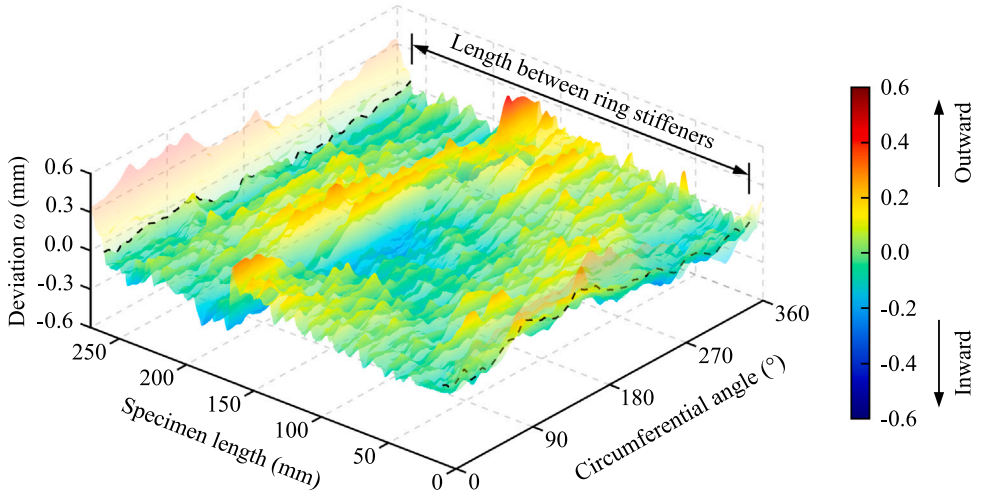


Fig. 15. Typical measured longitudinal imperfection distribution (specimen CS300).

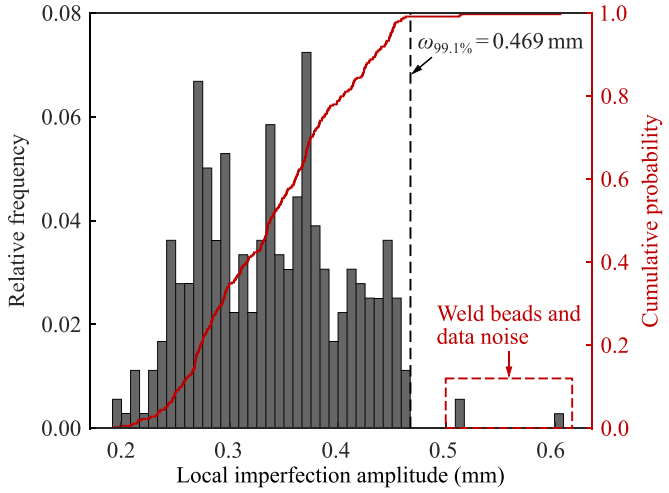


Fig. 16. Typical histogram and CDFs of longitudinal imperfections (specimen CS400).

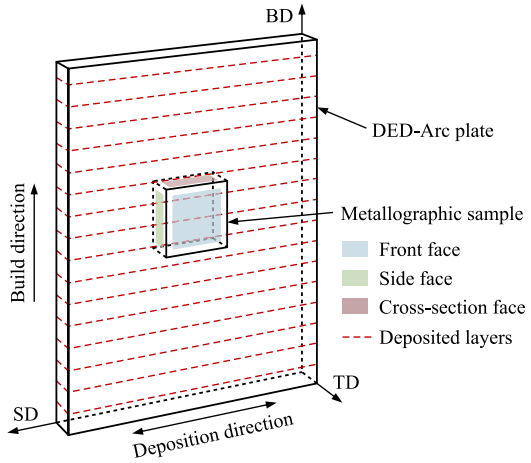


Fig. 17. Schematic illustration of the metallographic samples and their extraction locations.

The stress–strain curves obtained from the machined and as-built coupon tests are presented in Fig. 21. The obtained mechanical properties included the Young's modulus E, the Poisson's ratio ν, the yield strength f_y (taken as the 0.2% proof strength), the ultimate tensile strength f_u, the strain at the 0.2% proof strength ε_y, the strain at the ultimate tensile strength ε_u and the fracture strain measured over the marked standard gauge length ε_f [51]. A moving average filter of 10 points was applied to reduce the noise in the raw DIC data. The Young's modulus E was determined using least squares regression along the linear portion of the stress–strain curve, between approximately 10% and 40% of the yield strength f_y. Similarly, the Poisson's ratio ν was determined as the ratio of the mean transverse to the mean axial strains within the same elastic range. Note that the stress–strain curves and corresponding mechanical properties of the as-built coupons should be considered as 'effective' properties (as denoted by a subscript 'eff' in the notation) owing to the influence of the surface undulations.

Table 7
Average material properties of the machined coupons.

θ (°)	E (MPa)	ν (–)	f_y (MPa)	f_u (MPa)	ε_y (%)	ε_u (%)	ε_f (%)	$\frac{f_u}{f_y}$	$\frac{\varepsilon_u}{\varepsilon_y}$
0	203 300	0.286	954.9	1012.6	0.67	5.65	10.03	1.06	8.43
45	207 200	0.279	944.0	1023.3	0.66	4.09	7.16	1.08	6.23
90	206 100	0.280	948.7	1044.2	0.66	7.13	12.35	1.10	10.79

The average underlying (i.e. machined) and effective (i.e. as-built) mechanical properties are reported in Tables 7 and 8, respectively; the results for the individual specimens are given in Tables 9 and 10. In general, both the machined and the as-built coupons featured rounded stress–strain responses without a distinct yield point, as predicted by the criteria for the form of stress–strain curves set out in [76]. The Young's moduli and Poisson's ratios of the machined coupons, varying 200 GPa–208 GPa and 0.276–0.302, respectively, are similar to the typical values of conventionally-produced carbon steels [43]. The as-built coupons exhibited comparable Poisson's ratios to the machined coupons, ranging from 0.260 to 0.316, but slightly lower Young's moduli, ranging from 196 GPa to 207 GPa, owing to the slight weakening effect induced by the surface undulations. The obtained Young's moduli are similar to those reported by Chen et al. [61] and Huang et al. [71].

All machined specimens met the strength-based ductility requirement for hot-rolled high strength steel outlined in EN 1993-1-12:2007 [77], i.e. $f_u/f_y \geq 1.05$. Most of the as-built coupons also satisfied this requirement, with the exception of two 0° coupons, namely AB-0-2 and AB-0-3. In comparison with the nominal as-welded strength provided in the wire certificate (see Table 2), the material properties from both the machined and the as-built coupons generally

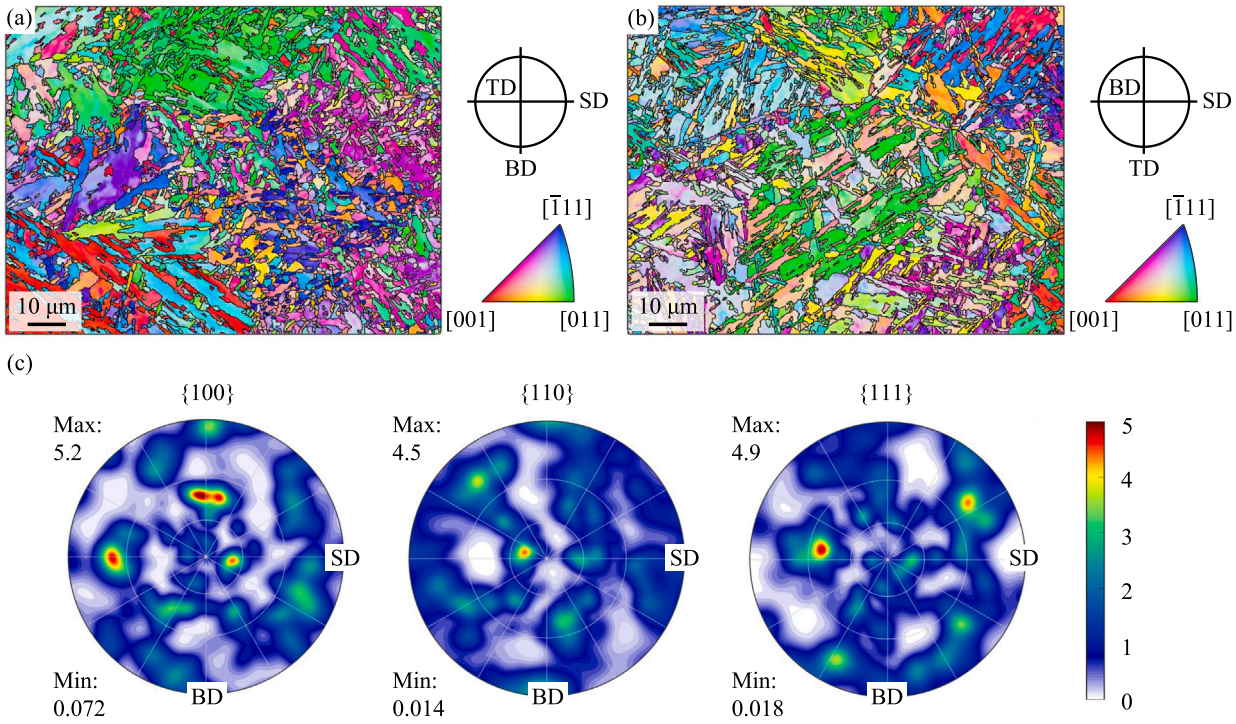


Fig. 18. (a) Inverse pole figures of the DED-Arc high strength steel samples in the (a) SD-BD (coloured relative to the build direction) and (b) SD-TD (coloured relative to the deposition direction) planes; (c) pole figures of the sample in the SD-BD plane.

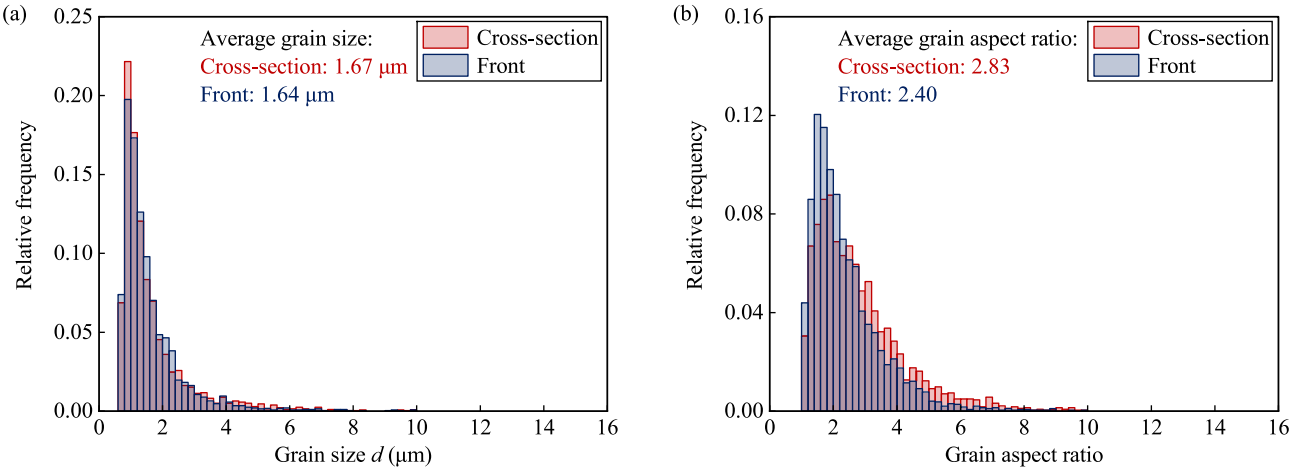


Fig. 19. (a) Grain size distribution and (b) grain aspect ratio distribution of examined DED-Arc high strength steel samples.

Table 8
Average effective material properties of the as-built coupons.

θ (°)	E_{eff} (MPa)	ν_{eff} (–)	$f_{y,eff}$ (MPa)	$f_{u,eff}$ (MPa)	$\varepsilon_{y,eff}$ (%)	$\varepsilon_{u,eff}$ (%)	$\varepsilon_{f,eff}$ (%)	$\frac{f_{u,eff}}{f_{y,eff}}$	$\frac{\varepsilon_{u,eff}}{\varepsilon_{y,eff}}$
0	200 100	0.291	938.2	984.6	0.67	5.52	9.64	1.05	8.26
45	201 400	0.278	902.8	985.4	0.65	4.81	9.26	1.09	7.42
90	200 200	0.284	870.1	974.1	0.63	4.64	6.63	1.12	7.32

satisfy the minimum guaranteed yield strength and the ultimate tensile strength, except for the 90° as-built coupons which exhibited a slightly lower yield strength than the guaranteed value. Regarding ductility, all coupons failed to reach the fracture strain specified in the wire certificate. However, the machined coupons generally met the requirement of $\varepsilon_f \geq 10\%$ specified in EN 1993-1-12:2007 [77], except for coupons M-0-4, M-0-5, M-45-1, and M-45-2. Notably, coupon M-45-1 experienced premature failure, owing to porosity, as indicated in Fig. 21(a). Most as-built coupons failed to meet the ductility requirement, particularly at higher θ angles, with all 90° as-built coupons exhibiting fracture strains below 10% [77]. Although this had negligible influence on the local buckling response of the tested stub columns, special attention should be given to other loading scenarios, such as flexure [62], combined compression and bending [28] and cyclic loading [78], where tensile strains may lead to premature fracture.

Figs. 22 and 23 show typical fractured machined and as-built coupons, accompanied by their corresponding surface axial strain fields at fracture as captured by the DIC process. The machined coupons exhibited fairly consistent strain patterns at fracture. The 45° and 90° as-built coupons exhibited noticeable axial strain localisations parallel

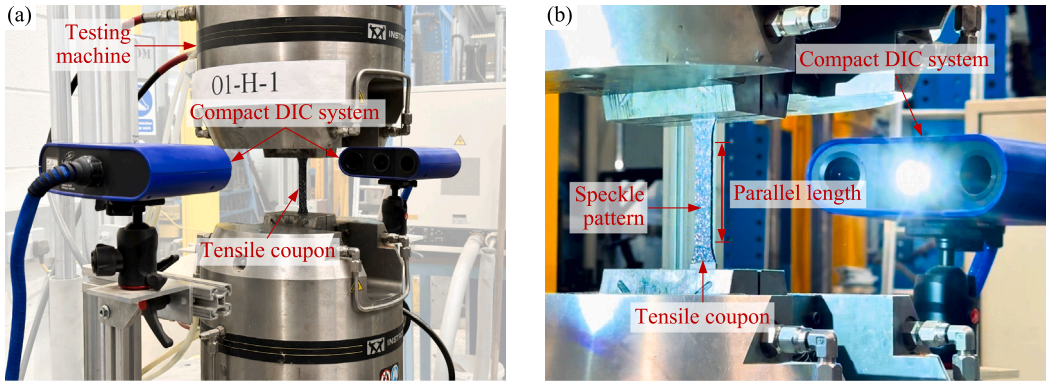
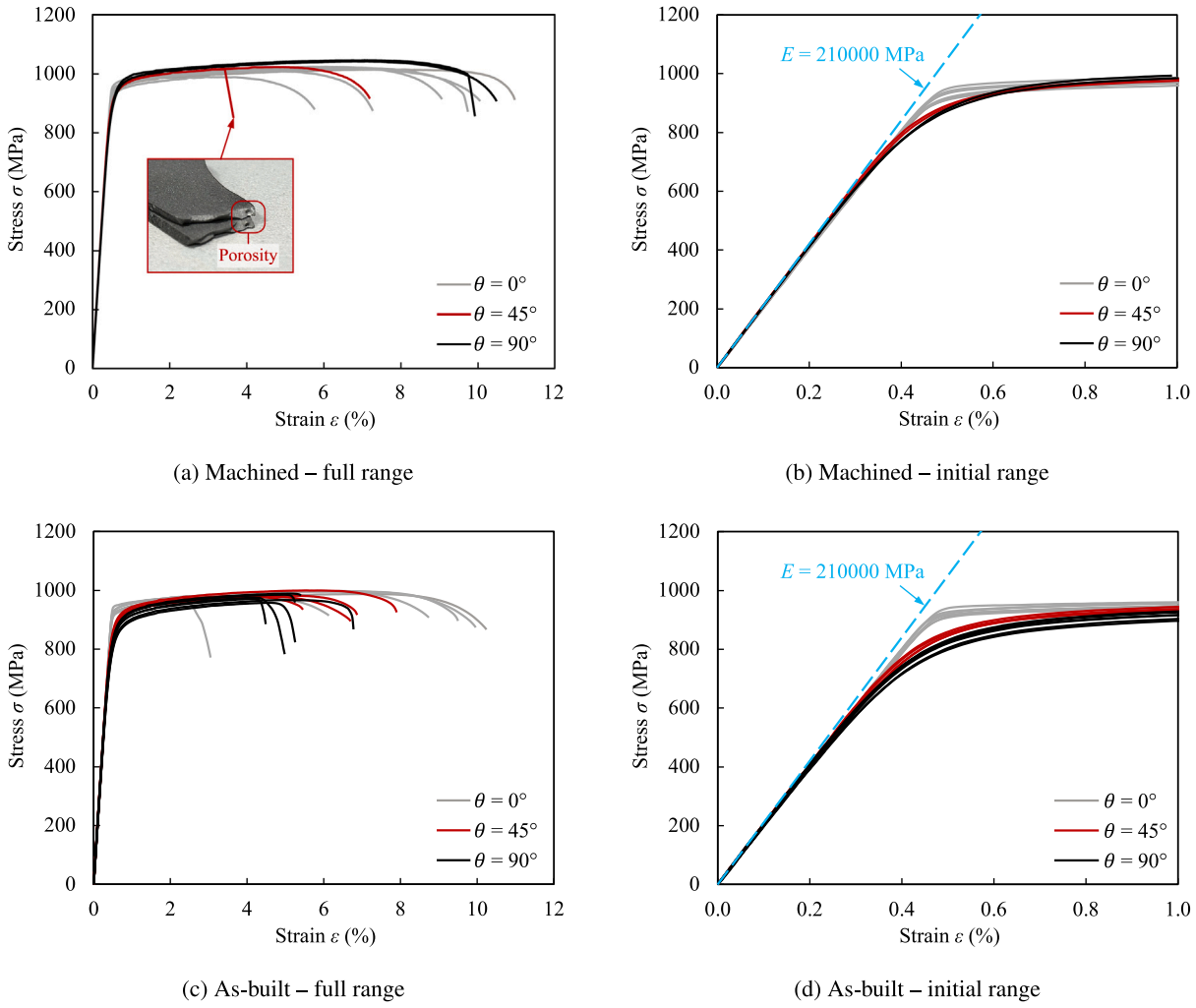


Fig. 20. Tensile coupon test setup: (a) overview; (b) close-up view.



(a) Machined – full range

(b) Machined – initial range

(c) As-built – full range

(d) As-built – initial range

Fig. 21. Stress–strain curves of the machined and as-built coupons.

to the deposition direction. In regions with smaller cross-sectional areas (i.e. in troughs), the material exhibited stress concentrations and thus early yielding, leading to premature loss of axial stiffness and more rounded stress–strain curves. Note that in the machined coupons with a small thickness (plane-stress), the coupling between tensile stress and shear stress [79] resulted in a failure direction of approximately 45°, as shown in Fig. 22.

4.3. Extent of material anisotropy

The individual and average mechanical properties of the machined and as-built coupons are plotted against the coupon orientation θ in Fig. 24. Both the machined and the as-built coupons exhibited nearly isotropic mechanical behaviour in the elastic range, which accords the weak crystallographic texture observed in the EBSD results, as described in Section 4.1. In the as-built coupons, a slight drop in the

Table 9
Material properties of the machined coupons.

Coupon ID	E (MPa)	ν (–)	f_y (MPa)	f_u (MPa)	ε_y (%)	ε_u (%)	ε_f (%)	$\frac{f_u}{f_y}$	$\frac{\varepsilon_u}{\varepsilon_y}$
M-0-1	200 400	0.283	945.1	1014.7	0.67	7.68	12.20	1.07	11.44
M-0-2	203 700	0.302	958.3	1017.0	0.67	6.64	11.53	1.06	9.91
M-0-3	205 500	0.279	962.0	1021.7	0.67	6.46	10.84	1.06	9.67
M-0-4	202 800	0.287	941.3	989.4	0.66	2.98	7.07	1.05	4.49
M-0-5	204 800	0.282	949.1	1009.0	0.66	4.05	8.49	1.06	6.11
M-0-6	202 400	0.285	973.4	1023.8	0.68	6.08	10.02	1.05	8.93
M-45-1	207 600	0.276	946.9	1024.0	0.66	3.26	6.20	1.08	4.97
M-45-2	206 800	0.282	941.0	1022.7	0.66	4.91	8.11	1.09	7.49
M-90-1	205 700	0.281	955.5	1046.4	0.66	7.13	12.89	1.10	10.73
M-90-2	206 500	0.278	942.0	1042.0	0.66	7.12	11.80	1.11	10.86

Table 10
Effective material properties of the as-built coupons.

Coupon ID	E_{eff} (MPa)	ν_{eff} (–)	$f_{y,eff}$ (MPa)	$f_{u,eff}$ (MPa)	$\varepsilon_{y,eff}$ (%)	$\varepsilon_{u,eff}$ (%)	$\varepsilon_{f,eff}$ (%)	$\frac{f_{u,eff}}{f_{y,eff}}$	$\frac{\varepsilon_{u,eff}}{\varepsilon_{y,eff}}$
AB-0-1	198 100	0.283	933.0	987.6	0.67	7.29	11.19	1.06	10.86
AB-0-2	197 100	0.260	926.9	956.4	0.67	2.39	5.49	1.03	3.57
AB-0-3	199 200	0.293	932.6	972.9	0.67	4.34	7.93	1.04	6.50
AB-0-4	202 600	0.316	942.4	997.8	0.67	6.51	10.62	1.06	9.79
AB-0-5	203 600	0.292	942.6	996.7	0.66	6.47	12.22	1.06	9.75
AB-0-6	200 100	0.301	951.6	996.4	0.68	6.14	10.38	1.05	9.09
AB-45-1	198 900	0.274	899.9	982.0	0.65	5.11	9.71	1.09	7.83
AB-45-2	198 300	0.281	901.1	978.8	0.65	4.63	8.80	1.09	7.07
AB-45-3	201 700	0.261	902.3	981.1	0.65	3.95	8.20	1.09	6.11
AB-45-4	206 700	0.295	907.9	999.7	0.64	5.55	10.33	1.10	8.69
AB-90-1	196 600	0.262	851.1	957.9	0.63	4.57	6.95	1.13	7.23
AB-90-2	201 700	0.287	874.9	970.6	0.63	4.19	5.54	1.11	6.62
AB-90-3	198 100	0.284	857.2	967.0	0.63	4.95	7.91	1.13	7.83
AB-90-4	198 100	0.301	873.8	974.8	0.64	4.11	6.47	1.12	6.41
AB-90-5	203 000	0.291	879.4	985.3	0.63	4.96	6.00	1.12	7.83
AB-90-6	203 700	0.284	884.5	989.1	0.63	5.07	6.93	1.12	7.99

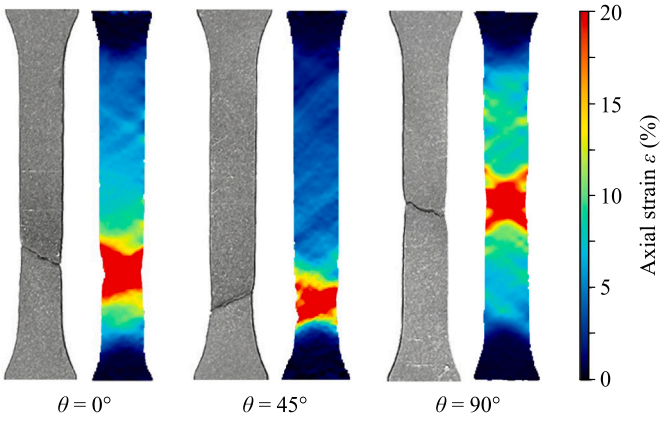


Fig. 22. Surface strains at fracture of typical machined coupons (i.e. M-0-2, M-45-2 and M-90-1).

yield and ultimate strengths can be observed as θ increases, owing to the increasing weakening effects of the undulating geometries (as θ increases, the geometric variability perpendicular to the load increases, and thus so do the local eccentricities). The results of the ultimate strains and the fracture strains exhibit greater variability compared to the Young's modulus, the Poisson's ratio, the yield strength and the ultimate tensile strength, as previously reported [80]. Overall, the tensile coupon test results, alongside the weak crystallographic texture reported in Section 4.1, indicate that the DED-Arc high strength steel exhibits nearly isotropic mechanical behaviour; similar observations have been made by Chen et al. [61] and Huang et al. [71].

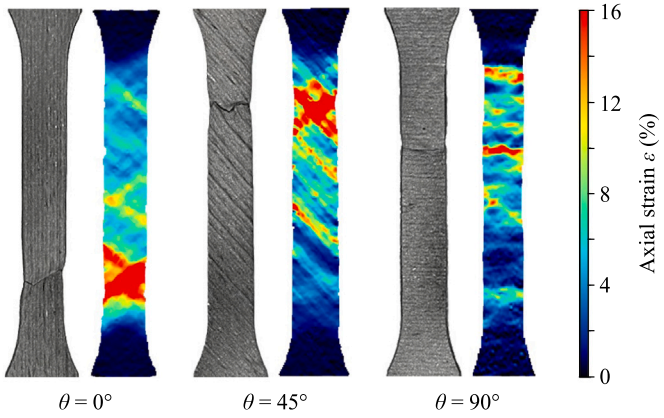


Fig. 23. Surface strains at fracture of typical as-built coupons (i.e. AB-0-6, AB-45-4 and AB-90-6).

Table 11
Comparison of average material properties between as-built and machined coupons.

θ (°)	$\frac{E_{eff}}{E}$	$\frac{\nu_{eff}}{\nu}$	$\frac{f_{y,eff}}{f_y}$	$\frac{f_{u,eff}}{f_u}$	$\frac{\varepsilon_{u,eff}}{\varepsilon_u}$	$\frac{\varepsilon_{f,eff}}{\varepsilon_f}$
0	0.98	1.02	0.98	0.97	0.98	0.96
45	0.97	1.00	0.96	0.96	1.18	1.29
90	0.97	1.02	0.92	0.93	0.65	0.54

4.4. Influence of geometric variability

The influence of the inherently undulating as-built geometry on the mechanical properties was evaluated by comparing the as-built with the machined coupon results. The ratios between the average effective (i.e. as-built) and the underlying (i.e. machined) mechanical properties are presented in Table 11. In the case of the Young's modulus and the Poisson's ratio, the ratios are consistently close to unity, indicating the minor influence of the undulations in the elastic range of the material response. However, differences of up to 8% can be observed in the case of the yield and ultimate strengths with the differences increasing with θ owing to the increasing geometric variability (as evidenced by the higher A_{sd}/A ratios presented in Table 4). Regarding the ultimate and fracture strains, the ratios of $\varepsilon_{u,eff}/\varepsilon_u$ and $\varepsilon_{f,eff}/\varepsilon_f$ of the 45° coupons are considered not representative, since their average ductility was significantly reduced by the premature failure of coupon M-45-1 due to porosity. In the case of the 90° coupons, significant reductions in the ultimate and fracture strains can be observed, with the differences reaching up to 35% and 46%, indicating a major negative effect of the geometric undulations on the ductility of the DED-Arc material.

5. Stub column tests

Twelve stub column tests were conducted on specimens with a wide range of diameter-to-thickness ratios to examine the cross-sectional behaviour of the DED-Arc CHS under axial compression over a wide range of cross-sectional slendernesses. Prior to testing, to avoid premature end failure [81] and to ensure fixed boundary conditions, the top and bottom edges of the CHS specimens were bonded to outer and inner high strength steel ring stiffeners with a thickness of 10 mm using Araldite 2011 reinforced epoxy adhesive [82], as shown in Fig. 25.

5.1. Test setup

The stub column tests were conducted using an Instron 3500 kN hydraulic testing machine; the test setup is shown in Fig. 26. The

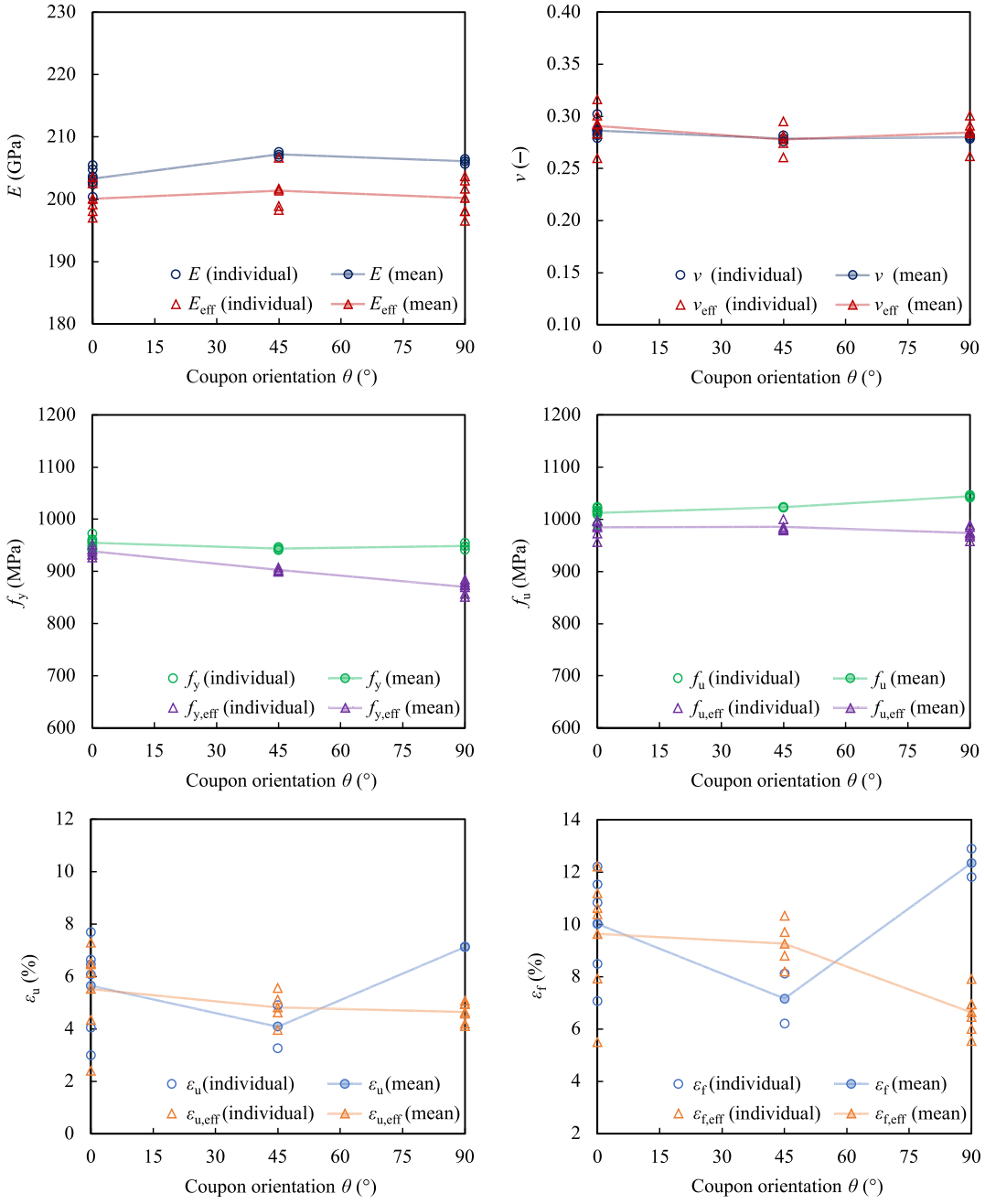


Fig. 24. Variation of key mechanical properties with coupon orientation for machined (circular markers) and as-built (triangular markers) DED-Arc coupons.

CHS specimens were placed between a pair of hardened high strength steel platens to avoid damage to the testing machine from the highly localised stresses. A ball seating was employed to accommodate any out-of-squareness of the specimen ends and thus ensure uniform axial loading. A four-camera stereoscopic LaVision DIC system [72] was utilised to monitor the three-dimensional displacement fields, as well as the end shortening on both sides of the test specimens. A random white speckle pattern was applied (on top of the spray-painted matt black background) onto the outer surface of the specimens. The tests were performed under displacement control at a compressive strain rate of 0.1% min^{-1}. The applied load and machine displacement data were recorded along with the DIC images at a frequency of 2 Hz and were processed using the software DaVis 10 [73].

5.2. Test results

The key test results are summarised in Table 12, where $D/t\varepsilon^2$ is the local slenderness (see Section 6.1), $\bar{\lambda}_c$ is the normalised cross-sectional slenderness (see Section 6.2), N_{pl} is the plastic load (calculated as the product of $A_{density}$ and the average yield strength f_y of the 90° as-built coupons), $N_{u,test}$ is the ultimate axial load, $\delta_{u,test}$ is the end shortening at the ultimate load, m is the observed number of meridional half-waves and n is the observed number of circumferential full waves in the asymmetric buckling mode. The average 90° mechanical properties were used in the design equations since the coupons had the same loading direction as the tested stub columns. In this manner, the weakening effects of the undulations, which, in both the 90° coupons and the stub columns, are perpendicular to the loading direction, are

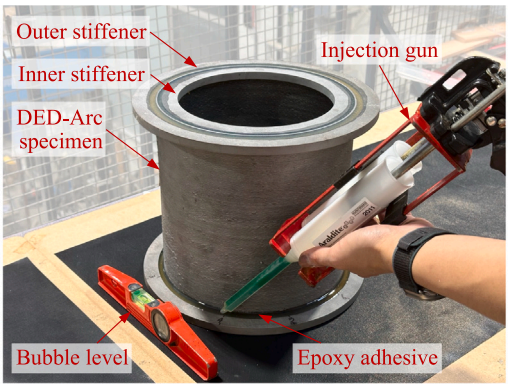


Fig. 25. Reinforcing of the ends of the DED-Arc CHS stub columns.

Table 12
Summary of the DED-Arc CHS stub column test results.

Specimen ID	$\frac{D}{t\varepsilon^2}$	$\bar{\lambda}_c$	N_{pl} (kN)	$N_{u,test}$ (kN)	$\delta_{u,test}$ (mm)	$\frac{N_{u,test}}{N_{pl}}$	Failure mode	m	n
CS20	34.3	0.18	102.8	142.6	7.37	1.387	Local bulge	–	–
CS30	51.8	0.22	161.1	201.0	4.13	1.248	Local bulge	–	–
CS40	68.9	0.25	219.0	260.6	2.20	1.190	Local bulge	–	–
CS55	97.8	0.30	304.2	349.1	1.51	1.148	Local bulge	–	–
CS80	142.8	0.36	448.6	498.1	1.29	1.111	Local bulge	–	–
CS110	199.4	0.43	620.9	664.3	1.26	1.070	Elephant foot	–	–
CS150	272.1	0.50	851.0	867.2	1.35	1.019	Diamond	2	3
CS200	363.2	0.58	1130.9	967.7	1.14	0.856	Diamond	2	5
CS250	460.8	0.65	1418.5	1145.2	1.31	0.807	Diamond	2	6
CS300	552.7	0.72	1706.5	1228.8	1.33	0.720	Diamond	2	6
CS350	630.4	0.77	2002.8	1224.0	1.28	0.611	Diamond	2	6
CS400	723.5	0.82	2298.6	1461.0	1.36	0.636	Diamond	2	7

taken into account; this approach has been successfully adopted in previous studies [26,30,83].

The axial load–end shortening curves obtained from the stub column tests are presented in Fig. 27, where N denotes the applied axial load and δ represents the end shortening as derived from the DIC data. To enable a direct comparison of the local buckling behaviour of the columns, the normalised form of the load–end shortening curves are plotted in Fig. 28, where the applied axial load is normalised by the plastic load N_{pl}, and the end shortening is normalised by the theoretical end shortening at first yield δ_y, as determined by Eq. (5):

$$\delta_y = \frac{f_y L}{E}, \tag{5}$$

where E is the Young's modulus corresponding to the 90° as-built coupons.

The initial slopes of the normalised load–end shortening curves align closely with the theoretical slope, as represented by the black dashed line in Fig. 28. However, increasing deviations are observed with increasing slenderness owing to the heightened sensitivity to the effects of residual stresses and initial local geometric imperfections [30]. Generally, the normalised load-carrying capacities of the cross-sections diminished with increasing slenderness ratio. The specimens with a nominal outer diameter exceeding 80 mm exhibited sharp unloading curves, which is indicative of unstable post-buckling, as generally associated with slender shells [52,84]. Notably, local buckling occurred abruptly in specimen CS400, leading to a sudden drop in the equilibrium path accompanied by a significant jump in the recorded end shortening values, as illustrated by the dashed lines in Figs. 27 and 28.

The failure modes of the DED-Arc CHS stub columns are presented in Fig. 29, where the inward deformations are highlighted with yellow dashed lines. Specimens with nominal outer diameters ranging from 150 mm to 400 mm exhibited failure owing to local buckling, characterised by an asymmetric 'diamond' pattern, featuring two meridional half waves and three to seven circumferential full waves, as detailed in Table 12. In contrast, the stockier cross-sections failed primarily owing to inelastic local buckling with outward bulges. Notably, specimen CS110 exhibited an 'elephant foot' buckling mode with an axisymmetric bulge at one end, whereas the other specimens exhibited spiral-like asymmetric local bulges at different locations along the specimen lengths; these latter observations are attributed to the non-uniformities within the specimens, including the geometric variabilities, imperfections, residual stresses and material heterogeneities inherent to the additive manufacturing process. To visualise the development of the axial strains and out-of-plane displacements in the case of the three typical failure modes observed herein, the equilibrium paths of specimens CS55 (local bulging), CS110 ('elephant foot' buckling) and CS400 ('diamond' pattern buckling) are shown alongside the DIC fields at different load levels in Fig. 30. Interestingly, in the case of specimen CS400, it can be seen that the shell jumped to a new equilibrium position immediately after reaching the ultimate load, and that the load–end shortening curve jumped onto a secondary equilibrium path. The out-of-plane DIC displacement fields illustrate the progression of the buckling shapes from an initial unstable 'chequerboard' pattern (with periodic waves of equal size) to a two-tier stable 'diamond' pattern featuring larger inward buckles and narrower outward ridges [40,85,86].

6. Assessment of existing design provisions

In the present section, the test data obtained from the stub column tests are used alongside test data collated from the literature to assess the applicability of existing design provisions, namely EN 1993-1-1:2022 [43] and EN 1993-1-6:2025 [44] to DED-Arc circular hollow sections in axial compression. The data collated from the literature comprises a total of 226 data points from tests on axially compressed steel CHS, including 175 cold-formed steel [62,64,87–102], 49 hot-rolled steel [64,81,89–91,103–110] and 2 DED-Arc steel CHS [42]. First, the design methods used for conventional CHS in axial compression, i.e. EN 1993-1-1 and EN 1993-1-6 are outlined. Then, the comparisons of the generated and collated test data with the design curves of EN 1993-1-1 and EN 1993-1-6 are made.

6.1. EN 1993-1-1:2022 provisions

According to EN 1993-1-1:2022 [43], cross-sections are categorised into four classes based on their susceptibility to local buckling [111,112]. In compression, Classes 1 to 3 cross-sections are considered to be fully effective, i.e. they can attain their full plastic resistance, while Class 4 cross-sections are slender, with local buckling causing failure to occur below the yield load. For CHS, the slenderness limit of Class 3 cross-sections is taken as 90 (i.e. $D/t\varepsilon^2 = 90$) [43]. The design resistance of cross-sections subjected to uniform compression $N_{c,Rd}$ is given by:

$$N_{c,Rd} = \begin{cases} \frac{A f_y}{\gamma_{M0}} & \text{for Class 1–3 cross-sections} \\ \frac{A_{eff} f_y}{\gamma_{M0}} & \text{for Class 4 cross-sections} \end{cases}, \tag{6}$$

where the cross-sectional area A is taken as $A_{density}$ for the DED-Arc CHS specimens herein, f_y is taken as the average yield strength of the 90° as-built coupons and γ_{M0} is the partial safety factor taken as unity; the effective area A_{eff} is given by:

$$A_{eff} = A\sqrt{\frac{90t\varepsilon^2}{D}} \quad \text{for } D/t\varepsilon^2 \le 240. \tag{7}$$

In Fig. 31, the ultimate loads from all the tests $N_{u,test}$ normalised by the plastic loads N_{pl}, are plotted against the local slenderness $D/t\varepsilon^2$,

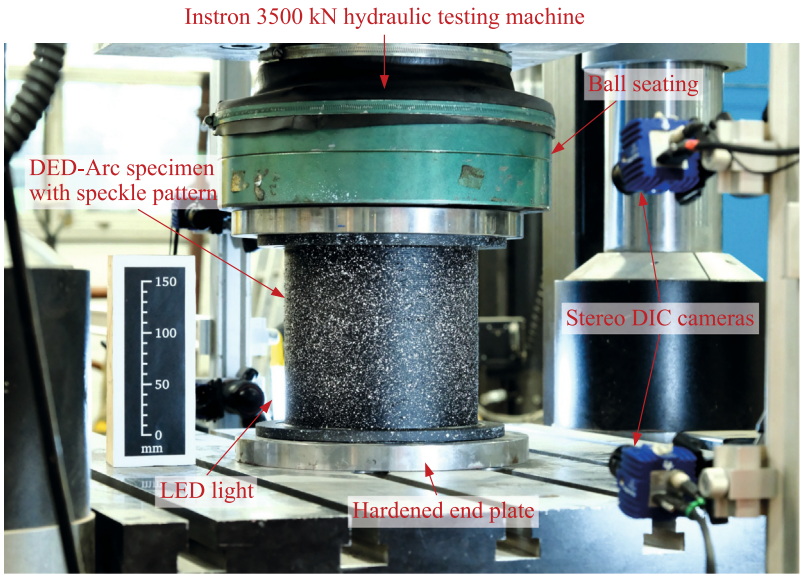


Fig. 26. DED-Arc CHS stub column test setup.

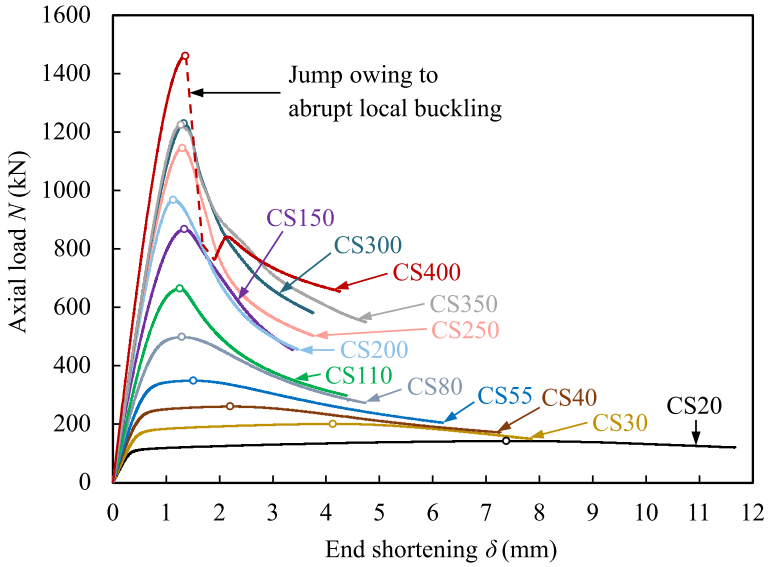


Fig. 27. load–end shortening curves obtained from the stub column tests; circular markers indicate the peak loads.

where the material parameter $\varepsilon = \sqrt{(235/f_y)\,(E/210000)}$ [43], along with the local bucking design curve, as set out in EN 1993-1-1 [43]. The inclusion of Young's modulus E in the material parameter ε is to account for the variation of E in the generated and collated test data. In general, the normalised load-carrying capacities (relative to the local slenderness) of the DED-Arc CHS can be seen to follow the trend of the collated cold-formed and hot-rolled steel CHS data from existing studies.

The ultimate loads obtained from the DED-Arc CHS stub column tests and the collated test results are normalised by the design predictions according to EN 1993-1-1, $N_{u,EC3\text{-}1\text{-}1}$, and are plotted against the local slenderness $D/t\varepsilon^2$ in Fig. 32. In the case of the DED-Arc CHS in this study, the predictions according to EN 1993-1-1 are shown to be overly conservative for the entire range of the examined local slenderness with all $N_{u,test}/N_{u,EC3\text{-}1\text{-}1}$ ratios exceeding 1.15, as shown in Table 13; the mean value of $N_{u,test}/N_{u,EC3\text{-}1\text{-}1}$ is 1.335, with the coefficient of variation (COV) of 0.116. The conservatism in the cases of the very stocky and slender DED-Arc CHS are attributed to the neglect of the strain hardening effects [113–115] and the low local buckling design curve [64], respectively.

6.2. EN 1993-1-6:2025 provisions

According to EN 1993-1-6 [44], as presented in Table 14, shells are classified into three length categories when designed under meridional (axial) compression, according to the dimensionless length parameter ω, given by:

$$\omega = \frac{L}{\sqrt{rt}}, \tag{8}$$

where L, r and t are the length, the shell middle surface radius and the shell thickness, respectively. The elastic critical meridional buckling stress $\sigma_{x,cr}$ is determined by:

$$\sigma_{x,cr} = \frac{C_x E}{\sqrt{3(1-\nu^2)}}\frac{2t}{D}, \tag{9}$$

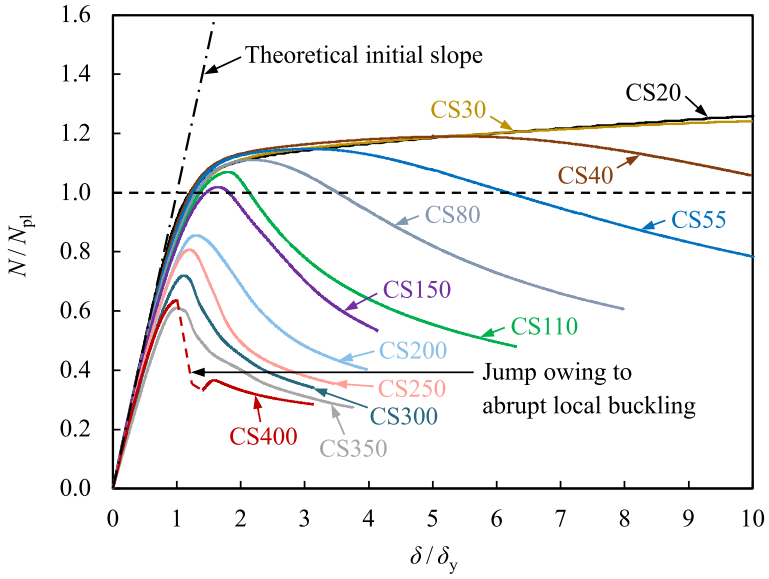


Fig. 28. Normalised load–end shortening curves obtained from the stub column tests.

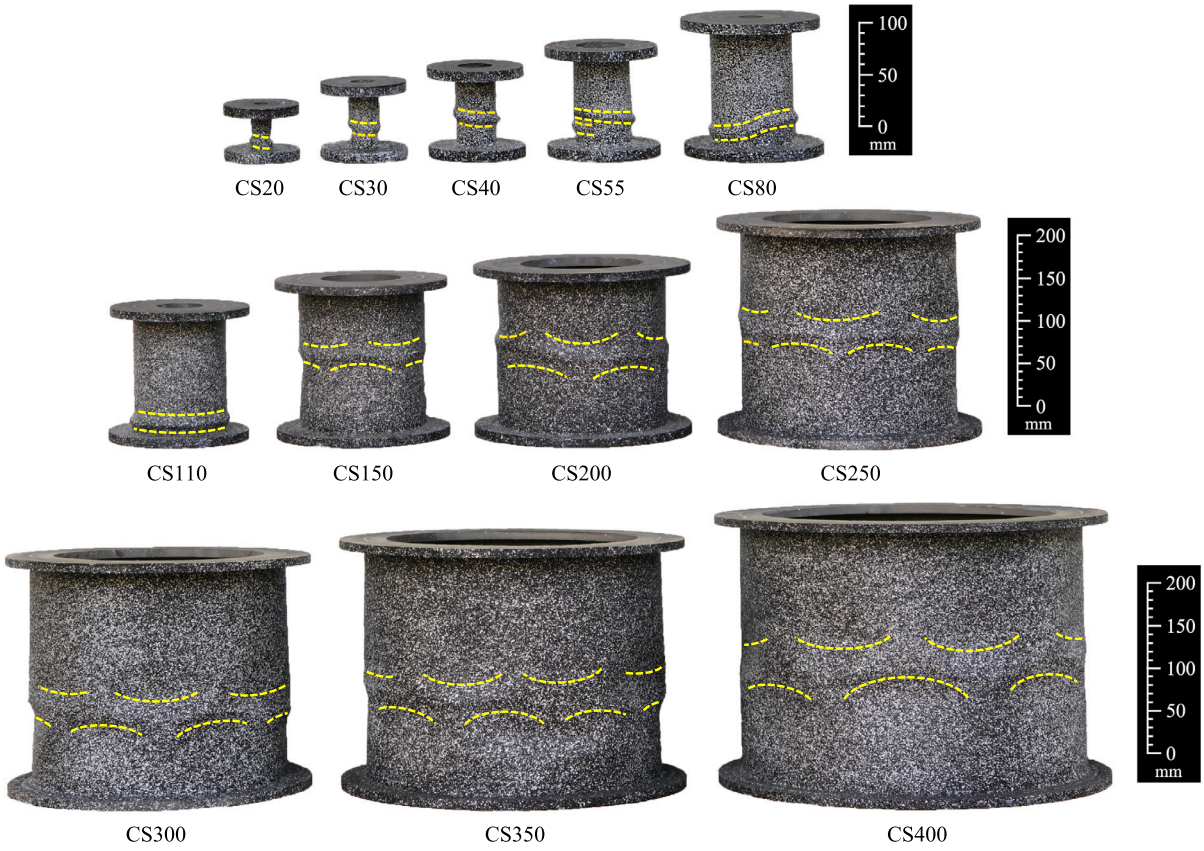


Fig. 29. Failure modes of the DED-Arc CHS stub columns; yellow dashed lines indicate inward deformations.

where the factor C_x scales the elastic critical buckling stress σ_{cr} for short cylinders according to the equations in Table 14.

According to EN 1993-1-6, the design buckling resistance is determined by accounting for the influence of membrane and bending effects, material plasticity and initial geometric imperfections. Thus, a generic design curve comprising three parts, to account for the plastic collapse, elasto-plastic buckling and elastic buckling, is employed, as outlined in Eq. (10):

$$\chi = \begin{cases} \chi_h - \dfrac{\bar{\lambda}_c}{\bar{\lambda}_0}\left(\chi_h - 1\right) & \text{when } \bar{\lambda}_c \le \bar{\lambda}_0 \\ 1 - \beta\left(\dfrac{\bar{\lambda}_c - \bar{\lambda}_0}{\bar{\lambda}_p - \bar{\lambda}_0}\right)^{\eta} & \text{when } \bar{\lambda}_0 < \bar{\lambda}_c < \bar{\lambda}_p \\ \dfrac{\alpha}{\bar{\lambda}_c^2} & \text{when } \bar{\lambda}_p \le \bar{\lambda}_c \end{cases}, \tag{10}$$

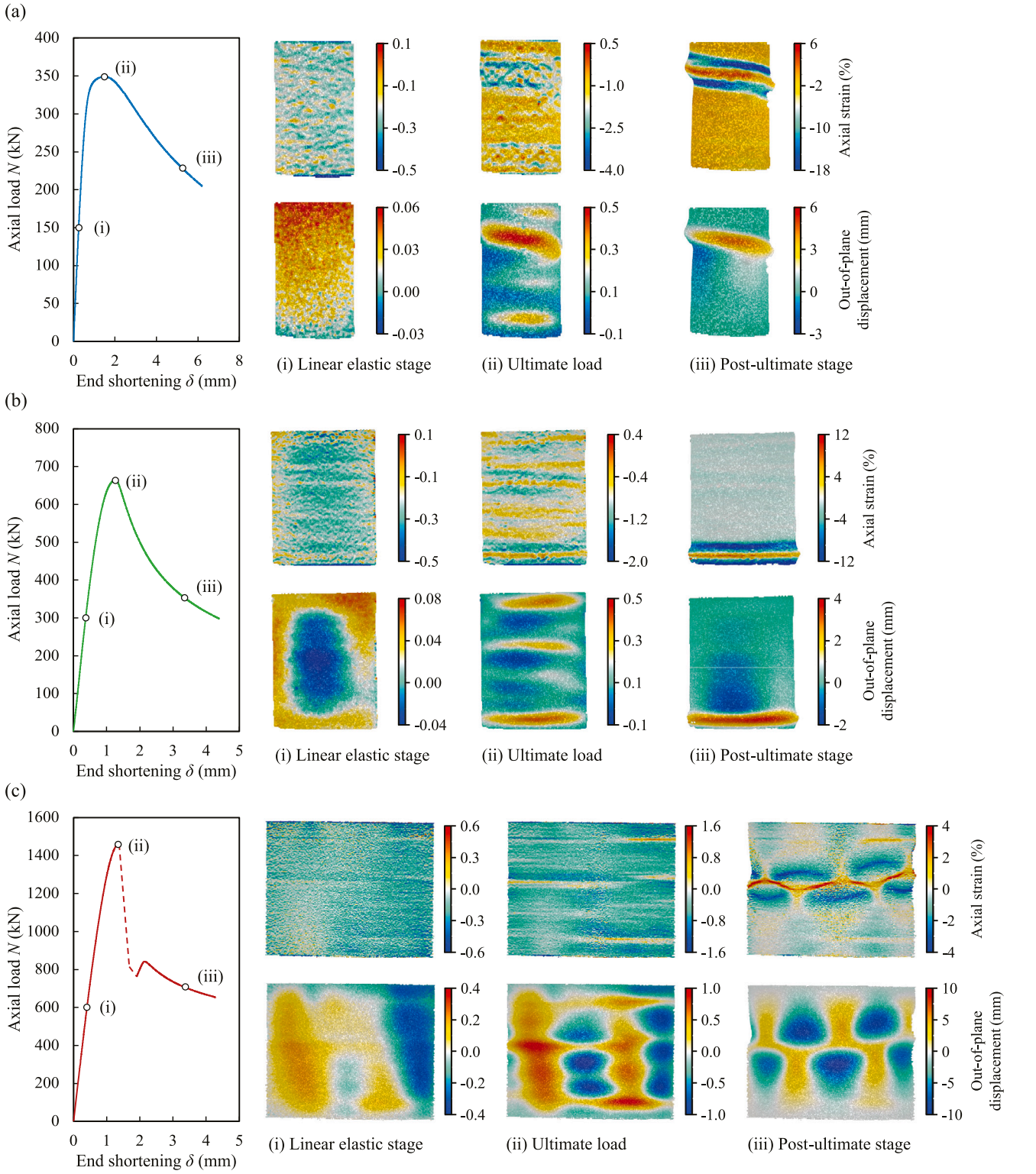


Fig. 30. Equilibrium paths, axial strain and out-of-plane displacement fields obtained from DIC for typical buckling modes at different load levels: (a) CS55 (local bulging), (b) CS110 ('elephant foot' buckling) and (c) CS400 ('diamond' pattern buckling).

where the buckling reduction factor χ is the ratio between the characteristic resistance R_k and the reference plastic resistance R_{pl}; the relative slenderness $\bar{\lambda}_c$ is equal to $\sqrt{f_y/\sigma_{x,cr}}$, where f_y is the material yield strength; χ_h is the hardening limit, $\bar{\lambda}_0$ is the squash limit relative slenderness, $\bar{\lambda}_p$ is the plastic limit relative slenderness, β is the plastic range factor, α is the elastic buckling reduction factor, η_0 is the value of η at $\bar{\lambda}_c = \bar{\lambda}_0$ and η_p is the value of η at $\bar{\lambda}_c = \bar{\lambda}_p$, as given in Table 15; η is the interaction exponent factor, as given by:

$$\eta = \frac{\bar{\lambda}_c\left(\eta_p - \eta_0\right) + \bar{\lambda}_p\eta_0 - \bar{\lambda}_0\eta_p}{\bar{\lambda}_p - \bar{\lambda}_0}. \tag{11}$$

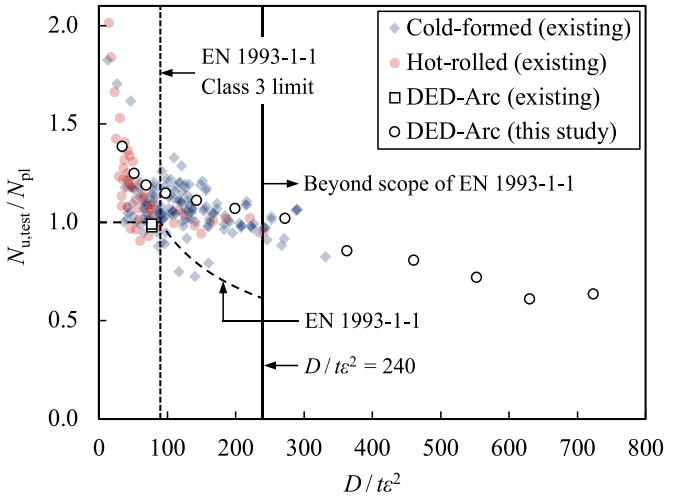


Fig. 31. Comparisons of the test results with the EN 1993-1-1 local buckling slenderness limits and design curve.

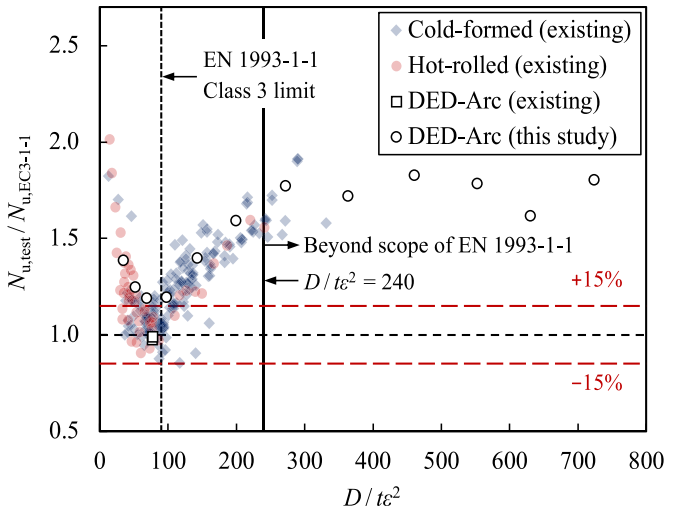


Fig. 32. Comparisons of the test results with the design predictions according to EN 1993-1-1.

Table 13
Summary of test results relative to design predictions (specimens marked with an * are beyond the scope of EN 1993-1-1).

Specimen ID	$\frac{D}{t\varepsilon^2}$	EC3-1-1 Class	$\bar{\lambda}_c$	$\frac{N_{u,test}}{N_{u,EC3-1-1}}$	$\frac{N_{u,test}}{N_{u,EC3-1-6}}$
CS20	34.3	1	0.18	1.387	1.403
CS30	51.8	2	0.22	1.248	1.270
CS40	68.9	2	0.25	1.190	1.219
CS55	97.8	4	0.30	1.196	1.189
CS80	142.8	4	0.36	1.399	1.186
CS110	199.4	4	0.43	1.593	1.172
CS150	272.1	4	0.50	–*	1.151
CS200	363.2	4	0.58	–*	1.025
CS250	460.8	4	0.65	–*	1.033
CS300	552.7	4	0.72	–*	0.973
CS350	630.4	4	0.77	–*	0.909
CS400	723.5	4	0.82	–*	0.957
Mean				1.335	1.124
COV				0.116	0.130

The geometric imperfection amplitude δ_0 (defined as $\sqrt{rt}/Q_\omega$, according to Eq. (4) is utilised in the determination of the buckling factors

Table 14
Parameters for determination of the elastic critical buckling stress for cylindrical shells with different lengths [44].

Length category	ω	C_x
Short	$\omega < 1.7$	$1.36 - \frac{1.83}{\omega} + \frac{2.07}{\omega^2}$
Medium-length	$1.7 \le \omega \le 1.43r/t$	1.0
Long	$\omega > 1.43r/t$	1.0

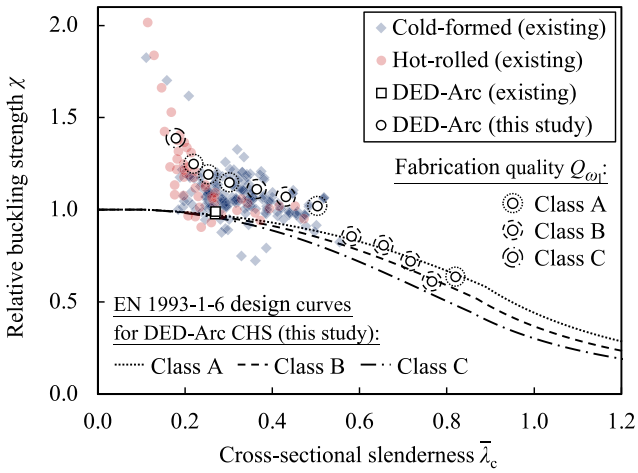


Fig. 33. Comparisons of test results with the EN 1993-1-6 design curves.

α, β, η_0 and η_p to consider the influence of geometric imperfections on the local buckling resistance. The parameter Q_ω represents the fabrication quality in meridional compression, which is taken as 40, 25 and 16 for Class A (excellent), Class B (high) and Class C (normal) shells.

The test data corresponding to the DED-Arc CHS test results and the data collated from the literature are plotted against the cross-sectional slenderness $\bar{\lambda}_c$ in Fig. 33; χ is the ratio of $N_{u,test}/N_{pl}$ for all the test data. The EN 1993-1-6 design curves for cylindrical shells with Classes A, B and C fabrication quality are also plotted. The average Young's modulus, Poisson's ratio and yield strength from the 90° DED-Arc as-built tensile coupons were used in creating the design curves. Note that the generated design curves are utilised to assess the performance of the DED-Arc CHS tested in this study only; for the collated data, the corresponding design curves are not provided due to the varying material properties and fabrication qualities. Generally, the data points of the examined DED-Arc high strength steel CHS stub columns are above the respective design curves of EN 1993-1-6, corresponding to safe-sided resistance predictions.

The test results of the DED-Arc CHS specimens, including those with reported local imperfection amplitudes from the literature, are compared with their corresponding EN 1993-1-6 predictions in Fig. 34. In the case of the DED-Arc CHS specimens, the imperfection amplitude δ_0 was taken as the measured local imperfection amplitude ω_1 (see Table 6), unlike in Fig. 33, where the limiting imperfection amplitudes for each quality class were used to plot the respective design curves for illustration purposes. For the results obtained from the literature, the geometric properties (i.e. D, t, L and ω_1) and material properties (i.e. E, ν and f_y) were taken as the reported values in the corresponding studies. It can be seen that the EN 1993-1-6 predictions are safe-sided up to local slenderness of 0.72, after which the $N_{u,test}/N_{u,EC3-1-6}$ ratio drops below unity. These unsafe predictions can be attributed to using the initial tangent modulus E_0 (i.e. Young's modulus) in resistance predictions for shells with materials exhibiting nonlinear stress–strain responses. In this study, the 90° as-built material exhibited

Table 15
Meridional buckling parameters from EN 1993-1-6 [44].

α	β	η_0	η_p	χ_{xh}	$\bar{\lambda}_0$	$\bar{\lambda}_p$
$\frac{0.83}{1+2.2\,(\delta_0/t)^{0.75}}$	$1-\frac{0.75}{1+1.1\,(\delta_0/t)}$	$1.35-0.10\,(\delta_0/t)$	$\frac{1}{0.45+0.72\,(\delta_0/t)}$	1.10	0.10	$\sqrt{\frac{\alpha}{1-\beta}}$

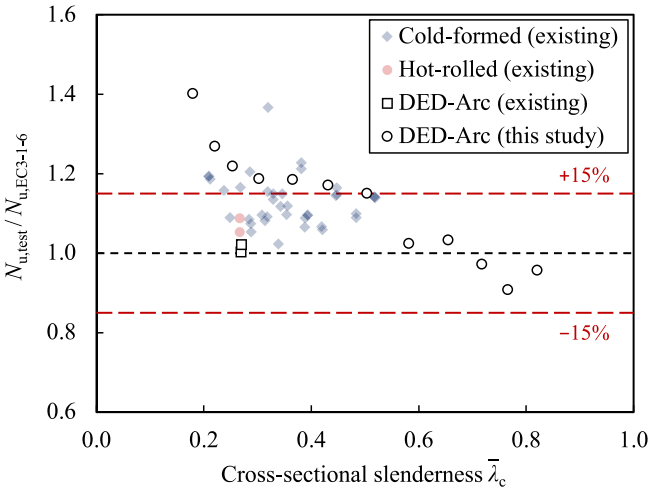


Fig. 34. Comparisons of test results with design predictions according to EN 1993-1-6.

a rounded stress–strain response between approximately $0.7f_y$ and f_y, falling below the idealised elasto-plastic material model (defined using E_0 and f_y) assumed in EN 1993-1-6 [44,116]. As a result, using E_0 underestimates the structural deformation of shells (particularly those of medium local slenderness), in which the average compressive stress lies within the rounded region of the stress–strain curve. This leads to premature buckling and thus non-conservative resistance predictions [116]. Similar findings have been reported for stainless steel cylindrical shells [52,84] and columns [117].

The $N_{u,test}/N_{u,EC3-1-6}$ ratios of the DED-Arc high strength CHS are listed in Table 13. Overall, as indicated by the mean value of $N_{u,test}/N_{u,EC3-1-6}$ of 1.124, it can be concluded that EN 1993-1-6 generally provided safe-sided predictions of the buckling resistance of the DED-Arc high strength steel CHS stub column examined herein. Compared with the EN 1993-1-1 predictions, EN 1993-1-6 yielded less conservative predictions, especially in the cases of specimens with slender proportions (i.e. Class 4 specimens: CS80–CS400). Further experimental work and numerical simulations are needed to obtain more data that could generalise the above conclusions for the design of DED-Arc shell structures.

7. Conclusions

A comprehensive experimental investigation into the local buckling behaviour of the wire-arc directed energy deposited (DED-Arc) high strength steel circular hollow sections (CHS) in compression has been conducted. Twelve DED-Arc CHS specimens were produced using ER120S-G wire and were examined at the microstructural, material and cross-sectional levels. Tensile coupons extracted at 0°, 45° and 90° orientations relative to the deposition direction provided the key mechanical properties of the examined DED-Arc material, revealing nearly isotropic material properties, as also indicated by the untextured microstructure observed through electron backscatter diffraction (EBSD) analysis. Prior to testing, 3D laser scanning was employed to capture the surface geometry of the tensile coupon and CHS specimens. Stub column compression tests were performed to investigate the local buckling behaviour of the DED-Arc CHS specimens and to determine their load-carrying capacities. During testing, digital image correlation was utilised to capture the deformation fields on the entire outer surface of the CHS specimens. All twelve CHS specimens exhibited local buckling failure; specifically, the six stockier (i.e. more compact) specimens exhibited inelastic local buckling with outward bulging or 'elephant foot' buckling, while the remaining more slender specimens failed in an asymmetric 'diamond' pattern buckling mode, that became more pronounced towards the ends of the tests. In general, the test results demonstrated a trend of decreasing load-carrying capacity with increasing local slenderness. The generated experimental data were utilised to assess the applicability of the current EN 1993-1-1 and EN 1993-1-6 provisions to the design of DED-Arc circular hollow sections in axial compression. The buckling resistance predictions based on EN 1993-1-1 were found to be somewhat conservative. In contrast, the buckling resistance predictions based on EN 1993-1-6, which incorporate the measured imperfection amplitudes, were generally safe-sided and reasonably accurate. The test results presented herein provide valuable experimental data and contribute in developing an understanding in the buckling behaviour of DED-Arc shell structures.

CRediT authorship contribution statement

Wenxuan Hong: Writing – original draft, Visualization, Validation, Software, Methodology, Investigation, Formal analysis, Data curation. **Ruizhi Zhang:** Writing – review & editing, Methodology, Investigation, Formal analysis, Data curation. **Nicolas Hadjipantelis:** Writing – review & editing, Supervision, Resources, Methodology, Investigation. **Leroy Gardner:** Writing – review & editing, Supervision, Project administration, Funding acquisition, Conceptualization.

Declaration of competing interest

The authors declare that they have no known competing financial interests or personal relationships that could have appeared to influence the work reported in this paper.

Acknowledgements

The authors gratefully acknowledge the Skempton Scholarship from Imperial College London, United Kingdom and the funding from the China Scholarship Council (CSC) for the financial support of the lead author. The authors would also like to acknowledge the support of the Robotic Construction Laboratory of the Department of Architecture of the University of Cyprus.

Data availability

Data will be made available on request.

References

[1] EN ISO/ASTM 52900:2021, Additive Manufacturing - General Principles - Fundamentals and Vocabulary, Standard, European Committee for Standardisation, Brussels, 2021.
[2] C. Huang, L. Li, N. Pichler, E. Ghafoori, L. Susmel, L. Gardner, Fatigue testing and analysis of steel plates manufactured by wire-arc directed energy deposition, Addit. Manuf. 73 (2023) 103696.
[3] L. Gardner, Metal additive manufacturing in structural engineering – review, advances, opportunities and outlook, Structures 47 (2023) 2178–2193.

[4] I.H. Shah, N. Hadjipantelis, L. Walter, R.J. Myers, L. Gardner, Environmental life cycle assessment of wire arc additively manufactured steel structural components, J. Clean. Prod. 389 (2023) 136071.

[5] X. Meng, L. Gardner, Standardisation framework for metal additive manufacturing in construction, Autom. Constr. (ISSN: 0926-5805) 176 (2025) 106267.

[6] F. Martina, J. Ding, S. Williams, A. Caballero, G. Pardal, L. Quintino, Tandem metal inert gas process for high productivity wire arc additive manufacturing in stainless steel, Addit. Manuf. 25 (2019) 545–550.

[7] T. Wang, N. Li, N. Yu, U. Mutilba, J. Flores, Y. Wang, P. Bartolo, S.K. Ong, Robot-assisted additive manufacturing for aerospace applications: Recent trends and its future possibilities, Int. J. Comput. Integr. Manuf. (2025) 1–41.

[8] STELIA Aerospace, World premiere for additive manufacturing: STELIA aerospace presents a demonstrator for metallic self-reinforced fuselage pannels manufactured by 3D impression, 2018, URL https://www.stelia-aerospace.com/wp-content/uploads/2018/02/CPStelia-DEFACTO_EN.pdf. (Accessed 31 July 2025).

[9] D. Chakraborty, T. Tirumala, S. Chitral, B.N. Sahoo, D.V. Kiran, P.A. Kumar, The state of the art for wire arc additive manufacturing process of titanium alloys for aerospace applications, J. Mater. Eng. Perform. 31 (8) (2022) 6149–6182.

[10] X. Zhang, C. Liu, H. Zeng, X. Jiang, S. Zhang, H. Zhou, H. Chai, X. Guo, Moving morphable components structural optimum approach considering wire arc additive manufacturing constraint and its application in satellite, Thin-Walled Struct. 192 (2023) 111177.

[11] T. He, S. Yu, R. Yu, B. Zheng, Oscillating wire arc additive manufacture of rocket motor bimetallic conical shell, Int. J. Adv. Manuf. Technol. 119 (9) (2022) 6601–6612.

[12] Relativity Space, Terran 1, 2023, URL https://www.relativityspace.com/glhf. (Accessed 31 July 2025).

[13] T. Blachowicz, G. Ehrmann, A. Ehrmann, Metal additive manufacturing for satellites and rockets, Appl. Sci. 11 (24) (2021) 12036.

[14] P. Kyvelou, A. Spinasa, L. Gardner, Testing and analysis of optimized wire arc additively manufactured steel trusses, J. Struct. Eng. 150 (3) (2024) 04024008.

[15] J. Yang, M.A. Wadee, L. Gardner, Strengthening of steel I-section beams by wire arc additive manufacturing – concept and experiments, Eng. Struct. 322 (2025) 119113.

[16] B. Weber, X. Meng, L. Gardner, Optimised and 3D printed steel garden bridge: from design to experimental verification, Autom. Constr., Autom. Constr. 181 (2026) 106638.

[17] X. Meng, L. Gardner, Hybrid construction featuring wire arc additive manufacturing: Review, concepts, challenges and opportunities, Eng. Struct. 326 (2025) 119337.

[18] L. Gardner, J. Li, X. Meng, C. Huang, P. Kyvelou, I-section steel columns strengthened by wire arc additive manufacturing-concept and experiments, Eng. Struct. 306 (2024) 117763.

[19] H. Dahaghin, M. Motavalli, H. Moshayedi, S.M. Zahrai, E. Ghafoori, Wire and arc additive manufacturing for strengthening of metallic components, Thin-Walled Struct. 203 (2024) 112074.

[20] M. Mavros, N. Hadjipantelis, I. Ioannou, O. Kontovourkis, A. Georgiou, In-plane strengthening of heritage masonry structures using 3D-printed steel reinforcement: Experimental proof-of-concept, Constr. Build. Mater. 499 (2025) 143746.

[21] J. Yang, M.A. Wadee, L. Gardner, Strengthening of hot-rolled S355 steel I-section beams using WAAM high strength steel, Thin-Walled Struct. 215 (2025) 113437.

[22] S.S. Song, J. Chen, J. Ye, G. Quan, Z. Wang, J. Xiao, Test and analysis of the interfacial bond behaviour of circular concrete-filled wire-arc additively manufactured steel tubes, J. Build. Eng. 82 (2024) 108171.

[23] J. Chen, S.S. Song, J. Ye, G. Quan, P. Kyvelou, L. Gardner, Axial compressive behaviour and design of concrete-filled wire arc additively manufactured steel tubes, Structures 70 (2024) 107495.

[24] W. Hong, S.I. Evans, K.A. Cashell, L. Gardner, N. Hadjipantelis, Stub column tests on concrete-filled wire arc additively manufactured steel tubes, in: International Colloquium on Stability and Ductility of Steel Structures, Barcelona, Spain, 8th September–10th September, 2025.

[25] S.I. Evans, F. Xu, J. Wang, Material properties and local stability of WAAM stainless steel equal angle sections, Eng. Struct. 287 (2023) 116160.

[26] S.I. Evans, N. Hadjipantelis, J. Wang, Stub column tests on wire arc additively manufactured equal-leg angle sections, Eng. Struct. 317 (2024) 118591.

[27] X. Chen, O. Zhao, F. Xu, J. Zhi, Y. Sun, Cross-sectional capacity of wire arc additively manufactured stainless steel channel section stub columns, J. Struct. Eng. 151 (6) (2025) 04025057.

[28] B. Weber, X. Meng, L. Gardner, Local buckling behaviour of wire arc additively manufactured steel I-sections under axial compression and combined loading, Thin-Walled Struct. 211 (2025) 113027.

[29] C. Huang, X. Meng, L. Gardner, Cross-sectional behaviour of wire arc additively manufactured tubular beams, Eng. Struct. 272 (2022) 114922.

[30] X. Meng, B. Weber, M. Nitawaki, L. Gardner, Optimisation and testing of wire arc additively manufactured steel stub columns, Thin-Walled Struct. 189 (2023) 110857.

[31] S.I. Evans, F. Xu, J. Wang, Experiments on the material and stability performance of slender WAAM plated structures, Thin-Walled Struct. 202 (2024) 112136.

[32] J.N. Dastgerdi, O. Jaberi, J. Hensel, Characterization of surface irregularities and fatigue strength evaluation of wire arc additive manufactured high strength steel specimens, Int. J. Fatigue 192 (2025) 108737.

[33] T.M. Chan, L. Gardner, K.H. Law, Structural design of elliptical hollow sections: A review, Proc. Inst. Civ. Eng. Struct. Build. 163 (6) (2010) 391–402.

[34] A. Espinos, L. Gardner, M.L. Romero, A. Hospitaler, Fire behaviour of concrete filled elliptical steel columns, Thin-Walled Struct. 49 (2) (2011) 239–255.

[35] A.I. Osofero, M.A. Wadee, L. Gardner, Experimental study of critical and post-buckling behaviour of prestressed stayed columns, J. Constr. Steel Res. 79 (2012) 226–241.

[36] Y. Zhong, O. Zhao, Experimental and numerical studies on post-fire behaviour of s700 high strength steel circular hollow sections under combined compression and bending, Thin-Walled Struct. 181 (2022) 110004.

[37] Y. Zhong, A. Su, O. Zhao, Post-fire local buckling behaviour of cold-formed s700 high strength steel circular hollow sections under axial compression: Experiments, modelling and design, Thin-Walled Struct. 184 (2023) 110511.

[38] Y. Zhong, K. Jiang, M.T. Chen, A. Su, O. Zhao, Local buckling of stainless steel stub columns with novel octagonal hollow sections, Eng. Struct. 338 (2025) 120512.

[39] N. Yamaki, Elastic Stability of Circular Cylindrical Shells, Elsevier, Amsterdam, 1984.

[40] J. Singer, J. Arbocz, T. Weller, Buckling Experiments: Experimental Methods in Buckling of Thin-Walled Structures, Volume 2: Shells, Built-Up Structures, Composites and Additional Topics, Vol. 2, John Wiley & Sons, 2002.

[41] V. Laghi, M. Palermo, G. Gasparini, V.A. Girelli, T. Trombetti, Experimental results for structural design of wire-and-arc additive manufactured stainless steel members, J. Constr. Steel Res. 167 (2020) 105858.

[42] M. Müggenburg, H. Jahns, K. Thiele, J. Müller, J. Hensel, J. Unglaub, Workflow for geometric evaluation, mechanical testing and simulation of DED-arc additively manufactured high-strength low-alloy steel components for local buckling, Structures 73 (2025) 108374.

[43] EN 1993-1-1:2022, Eurocode 3 - Design of Steel Structures - Part 1-1: General Rules and Rules for Buildings, Standard, European Committee for Standardisation, Brussels, 2020.

[44] EN 1993-1-6:2025, Eurocode 3 - Design of Steel Structures - Part 1-6: Strength and Stability of Shell Structures, Standard, European Committee for Standardisation, Brussels, 2025.

[45] N. Hadjipantelis, Wire arc additive manufacturing of steel structures: Guidelines and predictive equations, Structures 81 (2025) 110237.

[46] A. Joseph, D. Harwig, D.F. Farson, R. Richardson, Measurement and calculation of arc power and heat transfer efficiency in pulsed gas metal arc welding, Sci. Technol. Weld. Join. 8 (6) (2003) 400–406.

[47] L. Quintino, O. Liskevich, L. Vilarinho, A. Scotti, Heat input in full penetration welds in gas metal arc welding (GMAW), Int. J. Adv. Manuf. Technol. 68 (9) (2013) 2833–2840.

[48] ISO/TR 18491:2015, Welding and Allied Processes - Guidelines for Measurement of Arc Energies, Standard, European Committee for Standardisation, Brussels, 2015.

[49] EN 1011-1:2009, Welding - Recommendations for Welding of Metallic Materials - Part 1: General Guidance for Arc Welding, Standard, European Committee for Standardisation, Brussels, 2009.

[50] MX3D, MetalXL, 2024, URL https://mx3d.com/. (Accessed 14 August 2023).

[51] EN ISO 6892-1:2019, Metallic Materials - Tensile Testing - Part 1: Method of Test At Room Temperature, Standard, European Committee for Standardisation, Brussels, 2019.

[52] R. Zhang, M. Amraei, H. Piili, L. Gardner, Microstructure, mechanical properties and cross-sectional behaviour of additively manufactured stainless steel cylindrical shells, Thin-Walled Struct. 208 (2025) 112750.

[53] C. Huang, P. Kyvelou, R. Zhang, T.B. Britton, L. Gardner, Mechanical testing and microstructural analysis of wire arc additively manufactured steels, Mater. Des. 216 (2022) 110544.

[54] B. Weber, X. Meng, R. Zhang, M. Nitawaki, T. Sagawa, L. Gardner, Tensile behaviour of WAAM high strength steel material and members, Mater. Des. 237 (2024) 112517.

[55] W.D. Callister, D.G. Rethwisch, Fundamentals of Materials Science and Engineering, vol. 471660817, Wiley, London, 2000.

[56] FARO, FARO ScanArms, 2024, URL https://www.faro.com. (Accessed 31 July 2025).

[57] Oqton Inc, Geomagic wrap 2017, 2017, URL https://www.oqton.com/geomagic-wrap. (Accessed 31 July 2025).

[58] Robert McNeel & Associates, Rhino 6, 2018, URL https://www.rhino3d.com/. (Accessed on 31 July 2025).

[59] The Mathworks Inc, MATLAB:R2024a, 2024, URL https://uk.mathworks.com. (Accessed 31 July 2025).

[60] P. Kyvelou, H. Slack, D.D. Mountanou, M.A. Wadee, T.B. Britton, C. Buchanan, L. Gardner, Mechanical and microstructural testing of wire and arc additively manufactured sheet material, Mater. Des. 192 (2020) 108675.

[61] M. Chen, T. Zhang, Z. Gong, W. Zuo, Z. Wang, L. Zong, O. Zhao, L. Hu, Mechanical properties and microstructure characteristics of wire arc additively manufactured high-strength steels, Eng. Struct. 300 (2024) 117092.

[62] X. Meng, L. Gardner, Cross-sectional behaviour of cold-formed high strength steel circular hollow sections, Thin-Walled Struct. 156 (2020) 106822.

[63] R. Zhang, L. Gardner, C. Buchanan, V.P. Matilainen, H. Piili, A. Salminen, Testing and analysis of additively manufactured stainless steel CHS in compression, Thin-Walled Struct. 159 (2021) 107270.

[64] J. Nseir, Development of a New Design Method for the Cross-Section Capacity of Steel Hollow Sections (Ph.D. thesis), Department ArGEnCo, University of Liege, 2015.

[65] ASTM E3-11:2017, Standard Guide for Preparation of Metallographic Specimens, Standard, American Society for Testing and Materials, West Conshohocken, 2017.

[66] Oxford Instruments, AZtec, 2025, URL https://nano.oX.st.com/products/aztec. (Accessed 31 July 2025).

[67] F. Bachmann, R. Hielscher, H. SchaeB, Texture analysis with MTEX–free and open source software toolbox, Solid State Phenom. 160 (2010) 63–68.

[68] W. Hong, P. Kyvelou, R. Zhang, L. Gardner, Mechanical testing and microstructural analysis of wire laser beam directed energy deposited steel plates, Mater. Des. 255 (2025) 114141.

[69] A. Spinasa, B. Weber, X. Meng, R. Zhang, M. Nitawaki, L. Gardner, Influence of process parameters on the physical and material properties of WAAM steels, Constr. Build. Mater. 479 (2025) 141078.

[70] A. Kayadelen, H. Ateş, O. Yilmaz, Wire arc additive manufacturing (metal inert gas-cold metal transfer) of ER70s-6: Experimental and computational analysis on process, microstructure, and mechanical property relationships, J. Mater. Eng. Perform. 34 (2025) 1–17.

[71] C. Huang, N. Hadjipantelis, S. Quan, T. Chen, L. Gardner, Mechanical properties of wire arc additively manufactured steels at polar temperatures, Structures 70 (2024) 107627.

[72] LaVision GmbH, 2D-/3D stereo digital image correlation, 2025, URL https://www.lavision.de/en/. (Accessed 31 July 2025).

[73] LaVision GmbH, DaVis 10, 2021, URL https://www.lavision.de/en/products/davis-software. (Accessed 31 July 2025).

[74] X. Meng, L. Gardner, Testing of hot-finished high strength steel SHS and RHS under combined compression and bending, Thin-Walled Struct. 148 (2020) 106262.

[75] X. Guo, P. Kyvelou, J. Ye, L.H. Teh, L. Gardner, Experimental investigation of wire arc additively manufactured steel single-lap shear bolted connections, Thin-Walled Struct. 181 (2022) 110029.

[76] L.N. Dissanayake, F. Walport, X. Yun, L. Gardner, Unified stress–strain models for normal and high strength steels, Constr. Build. Mater. 459 (2025) 139616.

[77] EN 1993-1-12:2007, Eurocode 3 - Design of Steel Structures - Additional Rules for the Extension of EN 1993 Up to Steel Grades S 700, Standard, European Committee for Standardisation, Brussels, 2007.

[78] K.H. Nip, L. Gardner, A.Y. Elghazouli, Cyclic testing and numerical modelling of carbon steel and stainless steel tubular bracing members, Eng. Struct. 32 (2) (2010) 424–441.

[79] N. Hadjipantelis, B. Weber, C. Buchanan, L. Gardner, Description of anisotropic material response of wire and arc additively manufactured thin-walled stainless steel elements, Thin-Walled Struct. 171 (2022) 108634.

[80] B. Nie, S. Xu, Z. Zhang, A. Li, Surface morphology characteristics and mechanical properties of corroded cold-formed steel channel sections, J. Build. Eng. 42 (2021) 102786.

[81] M. Hayeck, Development of a New Design Method for Steel Hollow Section Members Resistance (Ph.D. thesis), Department ArGEnCo, University of Liege, 2016.

[82] Huntsman, Araldite 2011, 2025, URL https://www.huntsman.com/products/araldite2000/araldite-2011. (Accessed 31 July 2025).

[83] Ren Li, Andi Su, Yuyin Wang, Ou Zhao, Geometric analysis and local buckling behavior of wire arc additively manufactured er110s cruciform section stub columns, Eng. Struct. 322 (2025) 118819.

[84] R. Zhang, L. Gardner, M. Amraei, C. Buchanan, H. Piili, Testing and analysis of additively manufactured stainless steel corrugated cylindrical shells in compression, J. Eng. Mech. 149 (4) (2023) 04023013.

[85] T. Von Karman, H.S. Tsien, The buckling of thin cylindrical shells under axial compression, J. Aeronaut. Sci. 8 (8) (1941) 303–312.

[86] T. Kobayashi, Y. Mihara, F. Fujii, Path-tracing analysis for post-buckling process of elastic cylindrical shells under axial compression, Thin-Walled Struct. 61 (2012) 180–187.

[87] J.L. Ma, T.M. Chan, B. Young, Experimental investigation on stub-column behavior of cold-formed high-strength steel tubular sections, J. Struct. Eng. 142 (5) (2016) 04015174.

[88] M. Elchalakani, X.L. Zhao, R. Grzebieta, Tests on concrete filled double-skin (CHS outer and SHS inner) composite short columns under axial compression, Thin-Walled Struct. 40 (5) (2002) 415–441.

[89] J.G. Bouwkamp, Buckling and post-buckling strength of circular tubular sections, in: Offshore Technology Conference, OTC, Houston, 1975, pp. OTC–2204.

[90] M. Kato, T. Warizawa, T. Suzuki, T. Ogawa, Structural properties of high strength structural steel tubes, Trans. Iron Steel Inst. Jpn. 24 (2) (1984) 147–155.

[91] K. Ochi, B. Choo, Ultimate strength and post-buckling behaviour of CHS columns a comparison between cold-formed and hot-finished sections, in: Tubular Structures 5th International Symposium, Nottingham, 1993, pp. 163–170.

[92] H. Schmidt, Dickwandige kreiozylinderschalen aus stahl unter axialdruckbelastung, Der Stahlbau 58 (5) (1989) 143–148.

[93] S. Wei, S.T. Mau, C. Vipulanandan, S.K. Mantrala, Performance of new sandwich tube under axial loading: Experiment, J. Struct. Eng. 121 (12) (1995) 1806–1814.

[94] X.L. Zhao, Section capacity of very high strength (VHS) circular tubes under compression, Thin-Walled Struct. 37 (3) (2000) 223–240.

[95] H. Jiao, X.L. Zhao, Imperfection, residual stress and yield slenderness limit of very high strength (VHS) circular steel tubes, J. Constr. Steel Res. 59 (2) (2003) 233–249.

[96] K. Sakino, H. Nakahara, S. Morino, I. Nishiyama, Behavior of centrally loaded concrete-filled steel-tube short columns, J. Struct. Eng. 130 (2) (2004) 180–188.

[97] X.L. Zhao, L.W. Tong, X.Y. Wang, CFDST stub columns subjected to large deformation axial loading, Eng. Struct. 32 (3) (2010) 692–703.

[98] Y.F. Hu, M. Xiao, K.F. Chung, H. Ban, D.A. Nethercot, Experimental investigation into high strength S690 cold-formed circular hollow sections under compression, J. Constr. Steel Res. 194 (2022) 107306.

[99] J. Chen, T.M. Chan, A.H. Varma, Stub column behavior of cold-formed high-strength steel circular hollow sections under compression, J. Struct. Eng. 146 (12) (2020) 04020277.

[100] D. Wen, Y. Li, R. Peng, Y. Li, L. Wang, Y. Zhou, Investigation on the axial behavior of cold-formed thick-walled steel columns, J. Constr. Steel Res. 214 (2024) 108487.

[101] Y. Wei, Y. Guo, Q. Sun, B. Zhang, Study on local stability of Q690 high-strength steel tube under axial compression, China Civ. Eng. J. 46 (5) (2013) 1–12.

[102] Q.X. Ren, L.H. Han, D. Lam, C. Hou, Experiments on special-shaped CFST stub columns under axial compression, J. Constr. Steel Res. 98 (2014) 123–133.

[103] M.X. Xiong, D.X. Xiong, J.Y.R. Liew, Axial performance of short concrete filled steel tubes with high-and ultra-high-strength materials, Eng. Struct. 136 (2017) 494–510.

[104] Y. Toi, K. Yuge, K. Obata, Basic studies on the crashworthiness of structural elements (part 2) non-axisymmetric crush tests of circular cylinders and finite element analysis, J. Soc. Nav. Archit. Jpn. 1986 (160) (1986) 296–305.

[105] Y. Toi, T. Ine, Basic studies on the crashworthiness of structural elements (part 5) axisymmetric crush tests of circular cylinders and finite element analysis, J. Soc. Nav. Archit. Jpn. 1988 (164) (1988) 406–419.

[106] T. Kamba, Stub column test of high-strength CHS steel column with small diameter-to-thickness ratio, J. Struct. Constr. Eng. (Transactions AIJ) 507 (1998) 123–129.

[107] G. Giakoumelis, D. Lam, Axial capacity of circular concrete-filled tube columns, J. Constr. Steel Res. 60 (7) (2004) 1049–1068.

[108] J.G. Teng, Y.M. Hu, Behaviour of FRP-jacketed circular steel tubes and cylindrical shells under axial compression, Constr. Build. Mater. 21 (4) (2007) 827–838.

[109] U. Starossek, N. Falah, The interaction of steel tube and concrete core in concrete-filled steel tube columns, in: Tubular Structures XII, CRC Press, Shanghai, 2008, pp. 93–102.

[110] I. Tutuncu, T.D. O'Rourke, Compression behavior of nonslender cylindrical steel members with small and large-scale geometric imperfections, J. Struct. Eng. 132 (8) (2006) 1234–1241.

[111] L. Gardner, T.M. Chan, Cross-section classification of elliptical hollow sections, Steel Compos. Struct. 7 (3) (2007) 185.

[112] M. Bock, L. Gardner, E. Real, Material and local buckling response of ferritic stainless steel sections, Thin-Walled Struct. 89 (2015) 131–141.

[113] A. Liew, L. Gardner, Ultimate capacity of structural steel cross-sections under compression, bending and combined loading, Structures 1 (2015) 2–11.

[114] O. Zhao, L. Gardner, B. Young, Behaviour and design of stainless steel shs and rhs beam–columns, Thin-Walled Struct. 106 (2016) 330–345.

[115] L. Gardner, X. Yun, F. Walport, The continuous strength method – review and outlook, Eng. Struct. 275 (2023) 114924.

[116] J.M. Rotter, H. Schmidt, Buckling of steel shells – European design recommendations, in: European Convention for Constructional Steelwork, ECCS, Brussels, 2013.

[117] O. Zhao, L. Gardner, B. Young, Buckling of ferritic stainless steel members under combined axial compression and bending, J. Constr. Steel Res. 117 (2016) 35–48.